

DTIC FILE COPY  
AD-A223 613

2

AN ADVANCED SINGLE EVENT UPSET TESTER

by

Alfred G. Costantine

DTIC  
ELECTE  
JUL 03 1990  
S D S

A Thesis Submitted to the Graduate  
Faculty of Rensselaer Polytechnic Institute

in Partial Fulfillment of the Degree of

DOCTOR OF PHILOSOPHY

Major Subject: Nuclear Engineering

Approved by the  
Examining Committee:

Robert C. Block  
Robert C. Block, Thesis Adviser

Martin Becker  
Martin Becker, Member

Raymond D. Bellem  
Raymond D. Bellem, Member

Robert Hockenbury  
Robert Hockenbury, Member

Joseph M. Pimbley  
Joseph M. Pimbley, Member

Michael C. Stauber  
Michael C. Stauber, Member

DISTRIBUTION STATEMENT A

Approved for public release;  
Distribution Unlimited

Rensselaer Polytechnic Institute  
Troy, New York

August 1990

90 07 2 029

# REPORT DOCUMENTATION PAGE

Form Approved  
OMB No. 0704-0188

Public reporting burden for this collection of information is estimated to average 1 hour per response, including the time for reviewing instructions, searching existing data sources, gathering and maintaining the data needed, and reviewing the collection of information. Send comments regarding this burden estimate or any other aspect of this collection of information, including suggestions for reducing the burden, to Washington Headquarters Services, Directorate for Information Operations and Reports, 1215 Jefferson Davis Highway, Suite 1204, Arlington, VA 22202-4302, and to the Office of Management and Budget, Paperwork Project, Washington, DC 20503.

1. AGENCY USE ONLY (Leave Blank)		2. REPORT DATE MAY 1990	3. REPORT TYPE AND DATES COVERED FINAL	
4. TITLE AND SUBTITLE AN ADVANCED SINGLE EVENT UPSET TESTER			5. FUNDING NUMBERS	
6. AUTHOR(S) ALFRED G COSTANTINE				
7. PERFORMING ORGANIZATION NAME(S) AND ADDRESS(ES) DEPARTMENT OF Nuclear Eng. Rensselaer Polytechnic Institute TROY, NY 12186			8. PERFORMING ORGANIZATION REPORT NUMBER	
9. SPONSORING/MONITORING AGENCY NAME(S) AND ADDRESS(ES) USASD FORT BEN HARRISON, IN			10. SPONSORING/MONITORING AGENCY REPORT NUMBER	
11. SUPPLEMENTARY NOTES				
12a. DISTRIBUTION/AVAILABILITY STATEMENT AVAILABLE TO PUBLIC			12b. DISTRIBUTION CODE	
13. ABSTRACT (Maximum 200 words) THIS RESEARCH resulted in the building of a system to measure single event upset cross section versus linear energy transfer by using $^{252}\text{Cf}$ fission fragments in conjunction with thin film scintillators.				
14. SUBJECT TERMS SEU, Single Event Upset, SEU TESTING with $^{252}\text{Cf}$			15. NUMBER OF PAGES 104	
			16. PRICE CODE	
17. SECURITY CLASSIFICATION OF REPORT	18. SECURITY CLASSIFICATION OF THIS PAGE	19. SECURITY CLASSIFICATION OF ABSTRACT	20. LIMITATION OF ABSTRACT	

## CONTENTS

	Page
CONTENTS .....	ii
LIST OF TABLES.....	iv
LIST OF FIGURES.....	v
ACKNOWLEDGEMENT .....	ix
ABSTRACT .....	x
INTRODUCTION AND HISTORICAL REVIEW.....	1
The Single Event Problem and the Space Environment .....	1
Overview .....	1
The Cosmic Ray Environment .....	2
Current Testing Techniques .....	5
The Rensselaer Polytechnic Institute Advanced SEU Tester .....	8
Theory .....	10
Single Event Upset .....	10
Definition and Characterization .....	10
Mechanics of the Upset .....	16
The Funnel.....	18
Physical Analysis .....	20
Methods of SEU Protection.....	22
Californium-252 and the Fission Process .....	24
TFD Scintillation Theory .....	27
Stopping Power And Fission Fragments .....	36
MATERIALS AND APPARATUS.....	40
The Test Chamber .....	40

Data Collection Electronics .....	45
Nuclear electronics .....	45
Memory Tester .....	47
Interface .....	48
Data Collection And The Microcomputer .....	49
Thin Film Scintillator Preparation.....	49
EXPERIMENTAL METHOD .....	51
Thickness Measurements .....	52
Scintillator Versus SBD Calibration.....	55
The Overall SEU Cross Section .....	59
Determining the Individual SEU Cross Sections .....	60
Method of Determining LET.....	65
RESULTS.....	71
The Harris HM6516.....	72
The Honeywell HC6116CHEC.....	75
The IDT 6116.....	76
DISCUSSIONS AND CONCLUSIONS.....	79
Discussions.....	79
Conclusions.....	81
REFERENCES .....	84
APPENDIX.....	91



Accession For	
NTIS CRA&I	<input checked="" type="checkbox"/>
DTIC TAB	<input type="checkbox"/>
Unannounced	<input type="checkbox"/>
Justification	
By _____	
Distribution /	
Availability Codes	
Dist	Avail and/or Special
A-1	

## LIST OF TABLES

	Page
Table 1: Composition of cosmic rays.....	3
Table 2. Important Properties of $^{252}\text{Cf}$ .....	24
Table 3. Mean values of energy and mass for $^{252}\text{Cf}$ fission fragments. ....	27
Table 4. The measured thickness of scintillators and attenuators. ....	54
Table 5. Typical parameters for ions used in accelerator SEU testing .....	59
Table 6. Distribution and percentages for all scintillations and those that produce errors.....	61
Table 8. Essential data for the SEU cross section curve for the HM6516. These data are for the light-mass group.....	72
Table 9. Essential data for the SEU cross section curve for the HM6516. These data are for the heavy-mass group.....	73
Table 10. Essential data for the SEU cross section curve for the IDT 6116. These data are for the light-mass group.....	76
Table 11. Essential data for the SEU cross section curve for the IDT6116. These data are for the heavy-mass group.....	77

## LIST OF FIGURES

	Page
Figure 1. Composition of heavy ion cosmic ray spectrum as a function of atomic number.....	4
Figure 2. Typical layout for SEU testing at cyclotrons and accelerators. ....	6
Figure 3. LET distribution of $^{252}\text{Cf}$ fission fragments.....	7
Figure 4. Schematic of the advanced SEU chamber. ....	9
Figure 5. (a) DRAM schematic showing four information storage cells (b) Diagram of a vertical slice of a single MOS DRAM cell.....	11
Figure 6. Schematic of a bulk CMOS SRAM. The off transistors are the junctions that are sensitive to heavy ion strikes. The potential difference at these junctions collects the excess charge from the ion strike. ....	13
Figure 7. Scanning electron microscope photograph of heavy ion induced failure. This failure was induced by $^{252}\text{Cf}$ fission fragments. The small central core is around 100 nm to 200 nm in diameter.....	15
Figure 8. Response of a diode junction field to heavy ion penetration: (a) the ion penetrates and creates a column of electron-hole pairs; (b) the depletion layer collapses; (c) equipotential lines extend down the track. ....	17
Figure 9. Charge collection curves for a circuit array showing that the maximum charge is collected at the struck node due to funnelling. ....	19
Figure 10. The LRAM design.....	23
Figure 11. Mass and energy distributions for the spontaneous fission of $^{252}\text{Cf}$ . (a) the mass distributions as a function of fragment mass, $N(m^*)$ marks	

the pre-neutron-emission mass distribution, the post-emission mass distribution is unmarked. (b) the average single-fragment and total pre-neutron-emission kinetic energy as functions of mass .....	25
Figure 12. Potential energy function for deformations leading to fission.....	26
Figure 13. Contour plot of a correlated two parameter experiment on $^{252}\text{Cf}$ . Inserts show the summed spectra, over TFD and solid state detector contours, respectively.....	29
Figure 14. TFD response to degraded fission fragments showing pulse height distribution as a function of average fragment velocity.....	30
Figure 15. The relative light and heavy fragment peak pulse heights as a function of the fragment energy loss in the thin film scintillator. ....	31
Figure 16. A pictorial view of the recoil region, $P(R0,x)$ , available to the recoiled primary electrons. (a) The entire region of travel available to the recoil electrons. (b) The hatched region shows the area where p-electrons are excited. (c) Actual area calculated for ease of calculations .....	33
Figure 17. The calculated and experimental pulse height spectra of TFD for various film thicknesses. The solid lines are the calculated results while the histograms represent the experimental data from the scintillators.....	35
Figure 18. Energy loss per unit path length for fission fragments.....	36
Figure 19. Nuclear and electronic energy losses in Lindhard's dimensionless units. Actual values of $dE/dR$ and energy are indicated for fission fragments bombarding silicon.....	38

Figure 20. Electronic and nuclear stopping as determined from the computer code TRIM. Here Ba and Mo represent the typical heavy and light fission fragments bombarding silicon. ....	39
Figure 21. The SEU tester vacuum chamber. ....	40
Figure 22. A close-up of the source holding section. Push-pull rods allow the source to be moved from the exterior while the chamber is under vacuum. The blocking wheel shown can be replaced with a wheel of attenuators.....	41
Figure 23. A close-up of the chamber center section. This view is taken from the source location and shows that a fission fragment would pass through the light pipe openings, through the scintillator, and then onto the DUT.....	43
Figure 24. A close-up of the DUT card and surface barrier detector. ....	44
Figure 25. Electronic Equipment For the SEU System.....	46
Figure 26. Sample SEU cross section curve. ....	51
Figure 27. MCA pulse-height spectrum of unattenuated $^{252}\text{Cf}$ fission fragments as detected by the SBD.....	56
Figure 28. MCA pulse-height spectrum of $^{252}\text{Cf}$ fission fragments as detected by a TFD scintillator of $956 \mu\text{g}/\text{cm}^2$ thickness. ....	57
Figure 29. Calibration of a scintillator with the SBD. ....	58
Figure 30. The distribution of all scintillations (solid line) and those that caused errors (dashed line) for a total attenuation of $818 \mu\text{g}/\text{cm}^2$ .....	62
Figure 31. A composite of several data points that shows the effect of increased beam attenuation. The total thickness of the scintillator and attenuator	



material, in $\mu\text{g}/\text{cm}^2$ , is displayed in the upper right hand corner of each plot. ....	65
Figure 32. $dE/dx$ at the surface of silicon as determined by the TRIM computer code. Mo and Ba were chosen to represent the light-mass and heavy-mass fission fragments group respectively, then transported through scintillators of varied thickness using initial energies and masses as discussed in the text.....	68
Figure 33. Range of penetration into silicon for Mo and Ba after transport through scintillators of different thickness.....	69
Figure 34. SEU cross section versus LET curve for the HM6516. The error bars show the dispersion in LET. ....	74
Figure 35. The SEU cross section versus LET for the HM6516. The error bars show the standard deviation in the cross section.....	75
Figure 36. The SEU cross section versus LET for the IDT 6116. The error bars show the LET dispersion.....	77
Figure 37. The SEU cross section versus LET for the IDT 6116. The error bars show the standard deviation in the cross section.....	78
Figure 38. Dependence of measured cross section on ion species during exposure .....	80

### ACKNOWLEDGEMENT

The author wishes to express his sincere gratitude to Mr. Jim Kelly and Mr. Peter J. Brand, without whose constant help, interest, and technical expertise this research would not have been possible. A special thanks is extended to Dr. Jim Howard for the many enlightening discussions and for always being there to help. The hard work of Ms. T. Wu on the scintillator system is gratefully acknowledged. Mr. Ted Smith is deeply thanked for his help, encouragement, and technical discussions. Grumman Corporate Research is thanked for their support.

Finally, the author would like to especially thank Dr. Robert C. Block for his guidance and encouragement, and for teaching the author how to properly conduct research.

## ABSTRACT

Traditionally the testing of microelectronics for single event upset (SEU) sensitivity has involved actual exposure to the cosmic ray environment by high altitude flight programs or the simulation of the cosmic ray environment through the use of heavy ion beams produced by accelerators. These simulations are expensive and of limited access, thus alternatives have been sought.

This research resulted in the building of a system to measure single event upset cross section versus linear energy transfer by using  $^{252}\text{Cf}$  fission fragments in conjunction with thin-film scintillators. The first efforts to use  $^{252}\text{Cf}$  for SEU testing involved placing a  $^{252}\text{Cf}$  source in an evacuated chamber, bombarding the device under test, and calculating a single upset cross section that presumably was the saturation cross section. Such tests do not adequately address the uncertainties associated with the LET dispersion, and fail to usefully characterize the SEU threshold and saturation cross section of a device because there is no means to provide the SEU cross section versus LET curve. The system developed in this research effort addresses these shortcomings.

The key operational concept of this system is the ability to measure the energy of each heavy ion as it passes through a thin organic scintillator on the way to the device under test (DUT), and tag DUT upsets with the responsible fission fragment. Data analysis yields two distinct spectra, one of all fragment scintillation pulses and the other of those fragments that caused SEU. This ability to separate these spectra allows for the calculation of distinctly different upset cross sections for each energy group. Although this work determined upset cross sections for two energy groups, this technique can be readily extended to finer energy divisions for the californium spectrum.

The SEU cross section for several 2kx8 SRAM have been measured with this test device over the LET range from 17-43 MeV-cm<sup>2</sup>/mg. The saturation cross sections and

threshold LET values are in good agreement with the results from accelerator measurements. This californium-based device is quite small and fits onto a bench top. It provides a convenient and inexpensive supplement, or alternative, to accelerator and high-altitude SEU testing.

## CHAPTER 1

### INTRODUCTION AND HISTORICAL REVIEW

#### 1.1. The Single Event Problem and the Space Environment

##### 1.1.1. Overview

The goal of this research effort has been to design, construct, and demonstrate proof of principle for an advanced bench top apparatus to test for single event upsets (SEU) in microelectronics.

Advances in memory technology have led to increased packaging densities while power consumption has dropped. In general, such a trend has been beneficial to satellite and avionics technology except that a new mode of device failure has accompanied this miniaturization. In the near-Earth regions of space, harsh particle environments are always present in radiation belts, and occur sporadically at high latitudes due to solar flares and the galactic flux. In such high energy particle environments, microelectronic devices have been shown to be susceptible to upsets called single event upsets (SEU).<sup>1</sup>

Basically an SEU failure is an upset *to the information* stored in memory devices or the ability to interpret that *information* due to a disturbance in processing electronics. By definition, a single event upset is said to occur when a single highly ionizing particle produces a track of dense ionization in a semiconductor material and affects device operation through charge collection.<sup>2</sup>

Since high energy cosmic rays can easily penetrate several inches of aluminum, shielding against SEU is impractical. This factor and the increasing levels of integration and device miniaturization result in the susceptibility to soft errors being of increased concern to the military and aerospace communities.

The single event upset of a microprocessor involved in a space system can result in catastrophe. In addition to data register errors that are similar to soft errors in memory chips, a bit flip in a microprocessor can lead to a runaway processor. The runaway processor can overwrite random access memory (RAM) before ending up in an idle loop or coming to a complete halt. The end result of such an SEU is that system survival can be at stake. Thus the system designer must be aware of the SEU susceptibility of the components he uses and develop safeguards to insure mission success. To gain such knowledge testing must be done.

The testing of microelectronics for single event sensitivity traditionally has involved actual exposure to the cosmic ray environment by high altitude flight programs<sup>3</sup> or the simulation of the cosmic ray environment through the use of heavy ion beams produced by accelerators. These simulations are expensive and of very limited access, thus alternatives have been sought. Before examining the details of current testing programs and this work, it is essential to consider the cosmic environment that the SEU testing community hopes to simulate.

#### 1.1.2. The Cosmic Ray Environment

Based on source of origin and the nature of the upset mechanism, the particles that cause SEU can be grouped as cosmic ray heavy ions, cosmic ray protons, and packaging material heavy ions. Theories on the origin of cosmic ray particles indicate that they are thought to be inductively accelerated comparable to the acceleration of particles in a betatron. Rotating planetary bodies have rotational magnetic fields that generate rotational electric fields. The magnitude of the magnetic fields of a star allows particles to gradually accelerate to enormous velocities in the electric fields, while being held in closed paths. Once free from orbit, the mean free path of cosmic rays is  $10^8$  to  $10^9$  years as a consequence of the low density of interstellar matter. Table I delineates

the percentage breakout for the streams of high-energy nuclei that isotropically bombard the earth. The earth's magnetic field tends to alter the trajectory of the bombarding particles and influences the environment that orbiting satellites encounter.

Group of Nuclei	Charge	Flux Density [m <sup>-2</sup> -Sr <sup>-1</sup> s <sup>-1</sup> ]	Total Flux %
Protons	1	1300	92.90
Alpha particles	2	88	6.30
Light nuclei	3-5	1.9	0.13
Medium nuclei	6-9	5.6	0.40
Heavy nuclei	≥ 10	2.5	0.18
Super-heavy nuclei	≥ 20	0.7	0.05

Table 1: Composition of cosmic rays<sup>4</sup>.

Centered at approximately 2500-km above the earth the Van Allen belts consist mostly of protons plus electrons and other charged particles. Protons here can have enough energy to penetrate into a device and indirectly cause SEU. About one proton in every 10<sup>5</sup> has energy in excess of 30 MeV and can thus undergo nuclear reactions with the device material nuclei, thereby producing energetic charged particles that cause SEU. Such reaction particles include alphas, carbon ions, and actual fission of the silicon nucleus.<sup>5</sup>

The cosmic ray heavy ions often possess billions of electron volts of kinetic energy. This large amount of energy allows the particles to easily penetrate even thick shielding. Figure 1 shows the typical mass distribution for heavy ions in the cosmic environment. Note the peak at <sup>56</sup>Fe. Particularly important are the 100-MeV <sup>56</sup>Fe ions, with extremely high energy deposition per unit of track length, known as linear energy

transfer (LET), of  $27 \text{ MeV-cm}^2/\text{mg}$ . These  $^{56}\text{Fe}$  ions represent the most highly ionizing particles encountered in the cosmic environment. Any attempt to empirically simulate the cosmic environment must consider these ions.

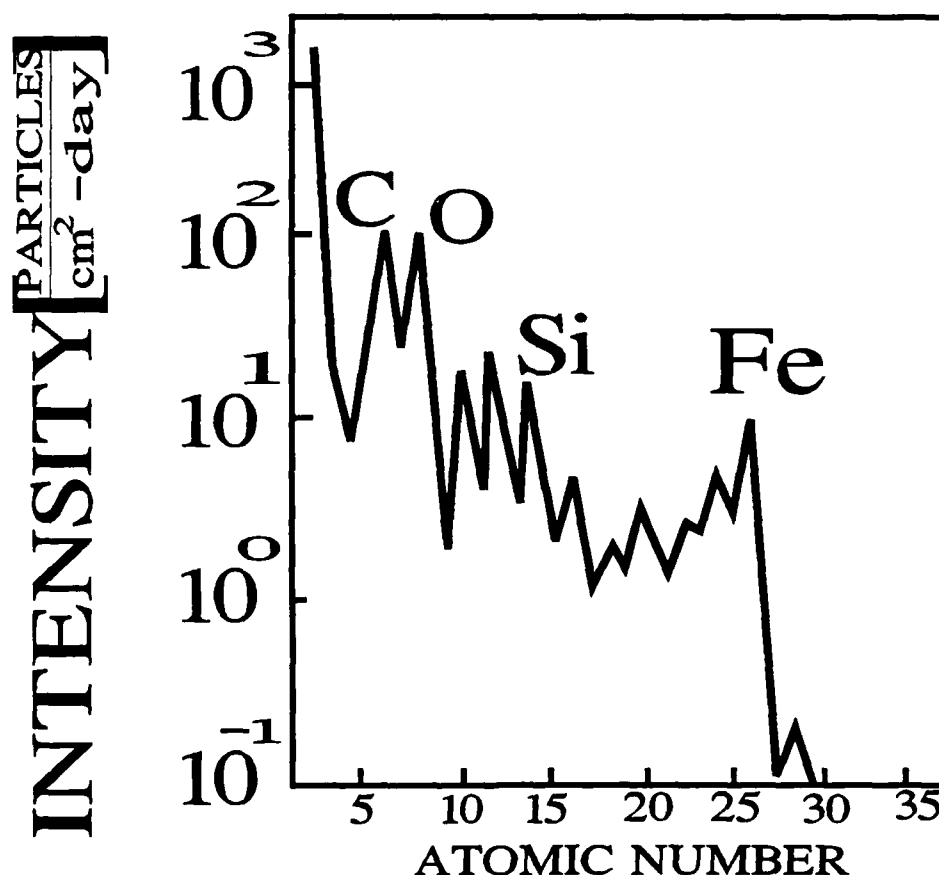


Figure 1. Composition of heavy ion cosmic ray spectrum as a function of atomic number.<sup>6</sup>

Finally, the material used to make the chip and its package may contain naturally occurring heavy actinide material (U, Th, and their daughters). These radioactive materials provide alpha particles that ionize the circuit materials and cause SEU. Alpha particles emitted in the header-package can be stopped from entering the chip by a simple passivation layer (a drop of polyimide varnish or silicon rubber) about the chip. However, those alpha particles originating with actinide decay in the chip material itself



cannot be similarly stopped. Additionally, heavy ion bombardment collisions with the silicon nuclei of the chip material can also produce alpha particles. A single alpha particle can produce about 3 million electron-hole pairs in silicon. This is enough charge to upset MOS-VLSI memory arrays. In fact, actinide concentrations of 1ppm can cause SEU degradations.<sup>5</sup>

### 1.2. Current Testing Techniques

SEU testing for complete device characterization requires the measuring of a device cross section as a function of ion LET or  $\frac{dE}{dx}$ , where the device cross section is expressed in terms of measured upsets per unit fluence and the LET is the amount of energy deposited along the path by an ion of known energy. The specific energy loss,  $\frac{dE}{dx}$ , is nearly identical to LET but also includes the energy released to delta rays; delta ray energy may travel a considerable distance from the particle track. Current laboratory efforts obtain heavy ions from machines similar to the Brookhaven tandem Van de Graaff accelerator and the U. C. Berkeley 88-inch cyclotron, or Californium-252 fission sources.

The tandem Van de Graaff accelerator at Brookhaven National Laboratory can provide the low energy, low atomic mass ions that are best suited for use in ascertaining the low LET threshold for more sensitive devices. Cyclotrons produce a variety of different heavy ions at a limited number of different energies. With energies available around 2 MeV per nucleon, ions can be chosen that have enough penetration to insure transit through the overlayers and into the active regions of delidded devices with sufficient LET to exceed that expected in the cosmic environment. The normal technique employed in these experiments is to direct a series of ion beams, each of specified energy, onto a device with a known pattern of information storage. Beam fluence and the number of errors are recorded and a single point on the upset cross

section versus LET curve is generated based on the ion LET at the device surface. Ion type and energies are varied to fully develop the SEU cross section curves. A schematic representation of a typical cyclotron test chamber is shown in Figure 2. Since the beam fluences used for SEU testing are several orders of magnitude lower than those normally supplied at accelerators, testers have developed their own dosimetry designed to count individual ions. The beam flux is measured by passing it through a thin film detector (TFD) made up of organic scintillation material. The light from the scintillator is conducted to a photomultiplier tube and counted. The ion energy is determined by the calibrated surface barrier detector (SBD) when it is positioned in the beam. A key feature of these chambers is the ability to vary particle LET by remotely positioning a selected device at desired angles in the beam through the use of a motorized translatable and rotatable board.<sup>7</sup>

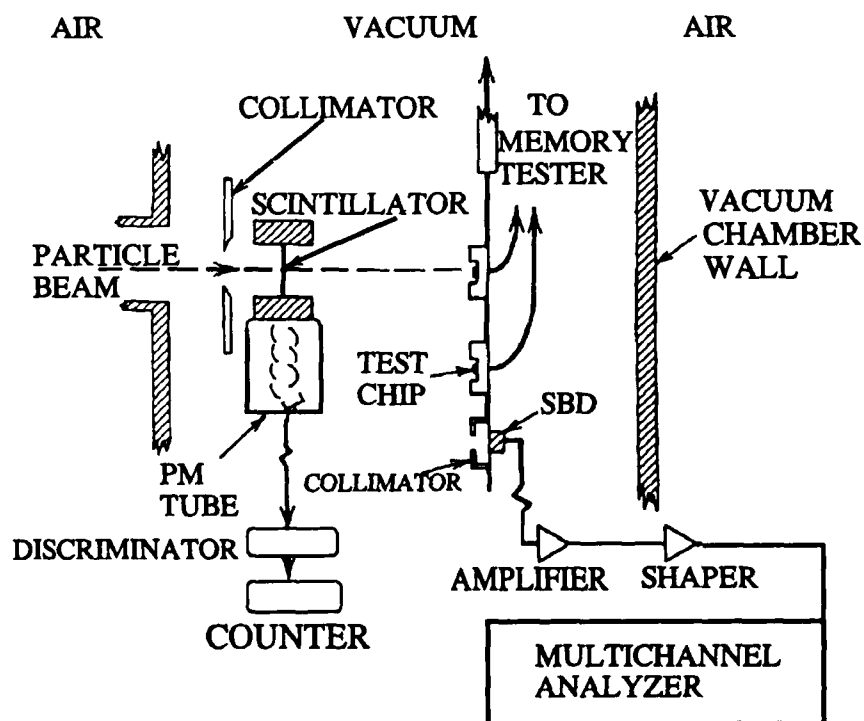


Figure 2. Typical layout for SEU testing at cyclotrons and accelerators.<sup>8</sup>

Van de Graaff accelerator and cyclotron test results comprise the bulk of the data available on SEU. However, access to these test facilities is limited and tests must be scheduled months in advance. Additionally, the cost of characterizing a single part runs from \$10,000 to \$100,000 depending on the complexity of the experiment.<sup>9</sup> Because of these drawbacks economical alternatives have been sought.

Since 100-MeV  $^{56}\text{Fe}$  ions, with LET of 27  $\text{MeV}\cdot\text{cm}^2/\text{mg}$  in silicon, represent the most highly ionizing particles encountered in the cosmic environment, acceptable testing sources must be able to provide these values as a minimum. Californium-252, with energies and LET that overlap these, was proposed as a cosmic ray simulator. Stephen et al.<sup>10</sup> showed that 95% of all  $^{252}\text{Cf}$  fission fragments have LET between 41 and 45  $\text{MeV}\cdot\text{cm}^2/\text{mg}$ , while 59.4% have LET between 43 and 44  $\text{MeV}\cdot\text{cm}^2/\text{mg}$  (see Figure 3).

#### Calculated LET Distribution of Cf-252 Fission Fragments

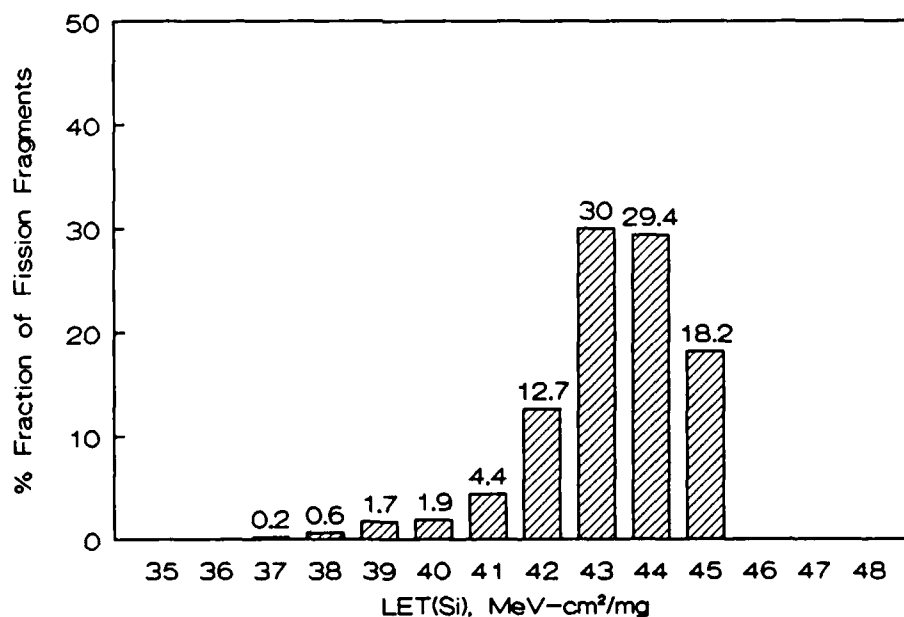


Figure 3. LET distribution of  $^{252}\text{Cf}$  fission fragments<sup>11</sup>.

By changing the angle of incidence or attenuating the fragment energies, effective LET from 20 to 75 MeV-cm<sup>2</sup>/mg can be realized.<sup>9,11</sup>

The first efforts to use <sup>252</sup>Cf for SEU testing involved placing a <sup>252</sup>Cf source in an evacuated chamber, bombarding the device under test (DUT), and calculating a single upset cross section that presumably was the saturation cross section<sup>12,13</sup>. Such tests do not adequately address the uncertainties associated with the LET dispersion<sup>14</sup>, and fail to usefully characterize the SEU threshold and saturation cross section of a device because there is no means to provide the SEU cross section versus LET curve.

Recent work by Browning<sup>10</sup> used air as an attenuator for <sup>252</sup>Cf fission fragments and developed the SEU cross section versus LET curves by unfolding the <sup>252</sup>Cf LET spectra by transporting all possible fission fragments through the air attenuator, the cover layers of the DUT, and the single-event sensitive layer. Such a technique means that the LET spectra must be calculated for each experimental variation and fails to account for the interaction of individual fission fragments while requiring extensive computer calculations.

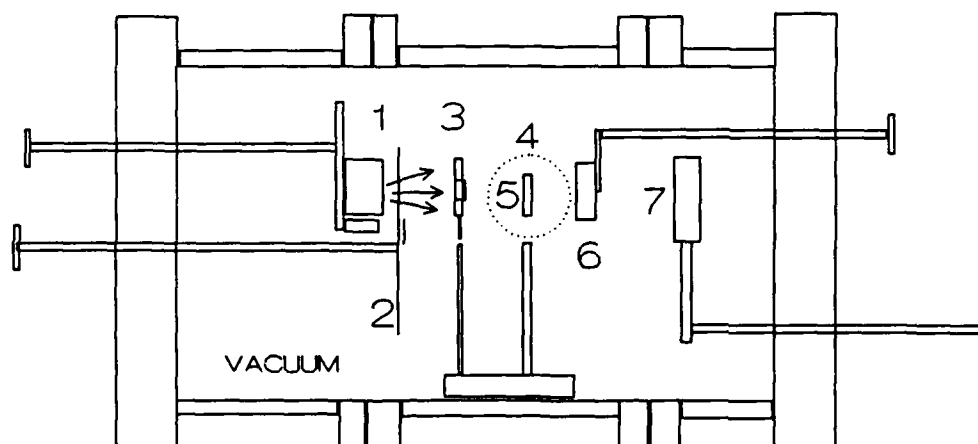
### 1.3. The Rensselaer Polytechnic Institute Advanced SEU Tester

This dissertation describes a new technique that uses thin film scintillators and <sup>252</sup>Cf to provide the capability to examine the energy and effect of each fission fragment that bombards a DUT. Such a technique results in an economical bench top apparatus that can be used to supplement or replace accelerator testing for SEU.

The key operational concept of the system is the ability to measure the energy of each heavy ion as it passes through a thin organic scintillator on the way to the DUT and associate DUT upsets with the responsible fission fragment. By determining the energy of each bombarding fission fragment, separate upset cross sections can be

calculated for different energy regions. Currently, this effort divides the spectrum into two groups, the heavy and light fission fragment groups.

### ADVANCED CALIFORNIUM SYSTEM FOR SEU TESTING



- 1) SOURCE    2) ATTENUATOR    3) IRIS    4) LIGHT PIPE  
5) SCINTILLATOR    6) SSD    7) DUT

Figure 4. Schematic of the advanced SEU chamber.

Figure 4 is a schematic of the system. The test chamber is basically a three-part vacuum chamber with electrical and mechanical feed throughs. A  $0.75 \mu$  Curie  $^{252}\text{Cf}$  source is used to provide fission fragments. A wheel of absorbers of different thickness varies the LET of the fission fragment spectrum. The scintillator film serves as a transmission detector which responds to the small amount of energy deposited by the particle as it passes through the film. The DUT is the particular device being characterized and is electrically wired to the tester outside the chamber. Greater details on component functions will be discussed in the theory and materials and apparatus sections that follow.

## CHAPTER 2

### Theory

#### 2.1. Single Event Upset

##### 2.1.1. Definition and Characterization

Let us first consider the basic characteristics of these upsets. The word "single" in SEU means that the error, or errors, produced can be attributed to a single ionizing particle impinging upon the device under consideration. Because of the natures of radioactive decay and the cosmic ray flux bathing the earth, SEU are random in both times of occurrence and positions within devices. However, we can define two basic types of upset, finite lifetime and permanent.

In finite lifetime upsets, commonly called soft errors, the stored information is changed but the associated hardware is not damaged or altered. When the cell that suffered such a logic upset is reset and tested, it exhibits no degradation in its characteristics. These finite upsets typically occur in fast random access memory (RAM).

Three failure modes for radiation induced soft errors in dynamic random access memories (DRAM) have been experimentally verified: the cell failure mode, the bit line failure mode, and combined cell-bit line mode. Figure 5(a) shows a schematic layout of a DRAM. The horizontal lines are known as word or select lines, while the vertical lines are known as bit or data lines. An access transistor and storage capacitor at the intersection of a word and a bit line comprise a single DRAM cell. The access transistor permits the support circuitry to locate the individual cells for reading or writing. Figure 5(b) shows that the storage capacitor is formed by using a thin layer of silicon dioxide as the dielectric. Writing occurs when the appropriate word line voltage is applied to the

gate of the access transistor while the bit line voltage is raised and charges the storage

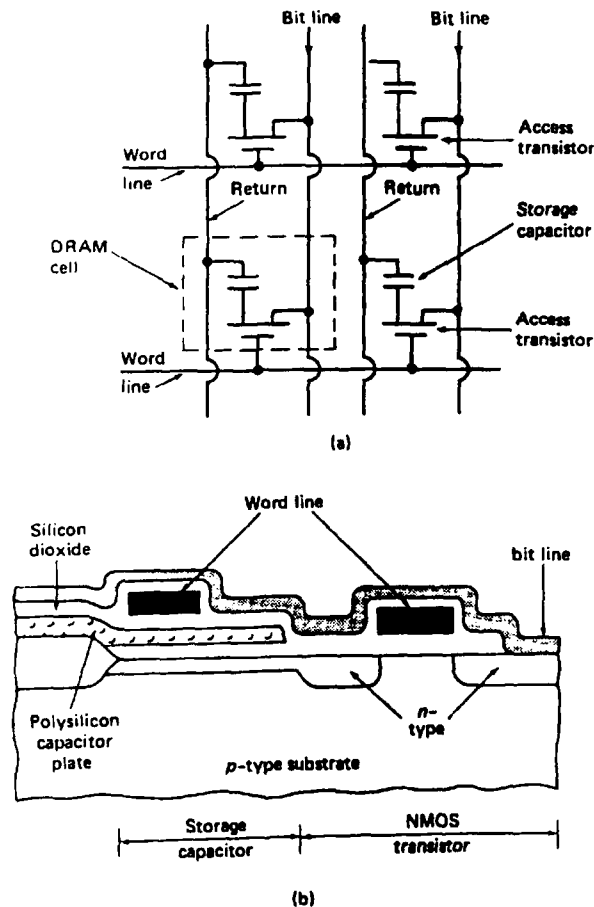


Figure 5. (a) DRAM schematic showing four information storage cells (b) Diagram of a vertical slice of a single MOS DRAM cell.<sup>5</sup>

capacitor. At the end of the write cycle the access transistor is returned to its off state. To read the DRAM the access transistor is turned on and the cell is connected to a sense and write amplifier that informs external circuitry of the cell's state and then restores the cell to its original state.<sup>5</sup>

The cell failure mode is the result of charge collection by the storage capacitor in the one-transistor cell. When the collected charge exceeds a critical charge,  $Q_{crit}$ , a soft error occurs in the cell.  $Q_{crit}$  is defined as the quantity of charge recognized as a binary 0 or 1 for the circuit of concern. The bit line failure occurs when charge collection causes a reduction in a sensing signal as a result of the unbalanced charge collection on a floating bit line or floating bit line complement during the access cycle. The actual charge collection results from the connection of the ion-caused-charge diffusion area to an access transistor. Recent studies<sup>15</sup> have revealed the third mode, combined cell-bit line. This failure occurs when the storage capacitor collects a charge less than  $Q_{crit}$ , and the bit line and bit line complement collect a differential charge less than  $Q_{crit}$ , while floating during a read cycle. Although the cell and bit line individual charge collections are insufficient to produce a soft error, if their combined charge collection is equal to or greater than  $Q_{crit}$ , an error can still result. At cycle times less than 100 nanoseconds this combined cell-bit line mode becomes the dominant mode for upset.<sup>15</sup> DRAM chips are inherently more susceptible to SEU than static RAM (SRAM) devices because there is no competing recovery mechanism attempting to restore the appropriate logical state.

SRAM devices use a bi-stable flip-flop formed by two cross-coupled inverters as the storage cell. Figure 6 is a schematic representation of a typical SRAM. In such a flip-flop the on transistor controls the gate voltage of the other transistor and keeps it in an off condition. When the off transistor is driven on by external means, it forces the on transistor to the off condition. Basically the flip-flop has two stable states and will, as long as power is applied to the circuit, remain in one of these states until forced to change. These states can be easily interpreted by external circuitry as a logical one or zero. The SEU of the SRAM can be thought of as a particle strike causing sufficiently





The permanent type of error, commonly referred to as hard error, is generally associated with combinatorial logic circuits. Once an error is transferred to such a bi-stable element it becomes permanent. This type of error has been found in the M6800 microprocessor.<sup>16</sup> Heavy ion induced hard errors result in stuck-at faults in microelectronic devices that can be attributed to the rupture of the gate dielectric as a consequence of the heavy ion passage. Wrobel's<sup>17</sup> studies of such hard failures for nonvolatile devices such as silicon-nitride-oxide-semiconductor (SNOS) and metal-nitride-oxide-semiconductor (MNOS) memory capacitors reveal the following:

- 1) Hard errors result from the energy directly deposited by the bombarding ion combined with the energy delivered by the electrical conduction through the ion track by the charge stored in the device.

- 2) The initial ion forms a highly conductive plasma that is five nanometers in diameter and the channel grows to 100 nanometers.

- 3) The total energy delivered by the initial ion strike must be sufficient to raise the dielectric temperature enough to cause the rapid thermal diffusion of the gate material and the subsequent penetration of the dielectric by this gate material. A scanning electron microscope (SEM) picture (Figure 7) of a failed device shows that the failure mechanisms are caused by dielectric penetration by either the aluminum or silicon. Additionally, the SEM photomicrographs show that the devices were locally raised to temperatures above the melting points of the constituent materials.

- 4) The post-failure I-V characteristics for these capacitors are similar to diode responses and some cases were simply ohmic shorts through the dielectric.

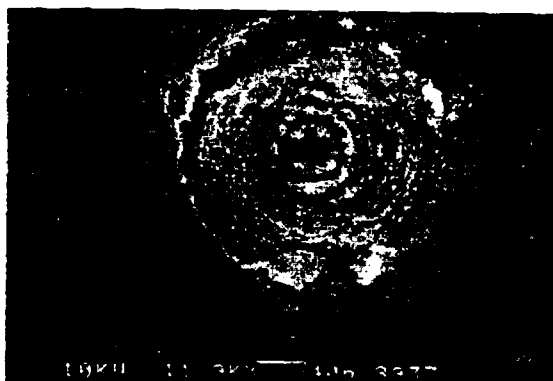


Figure 7. Scanning electron microscope photograph of heavy ion induced failure. This failure was induced by  $^{252}\text{Cf}$  fission fragments. The small central core is around 100 nm to 200 nm in diameter.<sup>18</sup>

To examine the possibility of melting the materials that make up these devices consider the following properties:

Material	Melting Temperature °C
Silicon	1412
Aluminum	660
Silicon Nitride	1900

The change in temperature,  $\Delta T$  can be calculated as:

$$\Delta T = \frac{\text{ENERGY}}{C_v (\text{VOLUME}) (\text{DENSITY})}$$

assume:

$$\langle \text{density} \rangle = 2.5 \text{ g/cm}^3$$

$$\text{track radius} = 2.5 \text{ nm}$$

$$\text{track length} = 80 \text{ nm}$$

$$C_v = 0.8 \frac{\text{J}}{\text{gm-}^\circ\text{C}}$$

$$\langle \text{LET} \rangle = 40 \frac{\text{MeV-cm}^2}{\text{mg}}$$

this leads to:

$$\Delta T = \frac{40 \frac{\text{MeV-cm}^2}{0.001 \text{ g}} (1.6 \times 10^{-13} \frac{\text{J}}{\text{MeV}}) (2.5 \frac{\text{g}}{\text{cm}^3}) (80 \times 10^{-7} \text{ cm})}{0.8 \frac{\text{J}}{\text{g-}^\circ\text{C}} [\pi (2.5 \times 10^{-7} \text{ cm})^2 (80 \times 10^{-7} \text{ cm})] (2.5 \text{ g/cm}^2)} = 40,743 \text{ }^\circ\text{C}$$

Using a track length of 80 nm allows 40 nm for the dielectric and 40 nm for the underlying silicon. This is consistent with Wrobel's estimates. This localized temperature rise only accounts the energy deposited by the heavy ion, conduction of stored charge through this plasma will increase this temperature rise. Such localized temperature rises support the premise of material melting.

### 2.1.2. Mechanics of the Upset

A highly ionizing particle, such as a 75-MeV heavy ion, that enters a semiconductor produces a track of very dense ionization. If this track passes through a critical node of an electronic apparatus, the device operation can be upset if sufficient charge is collected at the sensitive node. The upset process is known to depend on the properties of the ionizing track, the density of the electron-hole pairs formed in its wake, the angle of track entrance, the proximity of sensitive nodes, device structure and material properties. The charge collection process and time scales of this collection are essential in determining the extent of the SEU problem and the subsequent upset rates.

Thus the ionization process results in charge separation and its subsequent collection within a device. To understand how this results in errors we again consider the concept of device critical charge. The critical charge is the amount of charge that a system recognizes as binary 1 or 0 at a particular storage node in a memory array. For a

DRAM operating at 5 volts, the greatest voltage swing that can be withstood without losing stored information is about 2.5 volts. If the storage capacitance is 50 fF, then:

$$Q_c = C_{st} V_{crit} = 50 \times 10^{-15} \text{ F} \times 2.5 \text{ V} = 125 \text{ fC} = 7.8 \times 10^5 \text{ electrons.}$$

To put this in perspective consider that the total number of electron hole pairs generated in silicon by a 5 MeV alpha particle is around  $1.5 \times 10^6$ . This problem is exacerbated when devices are scaled down because smaller capacitors have smaller capacitance values. Because of scaling, more advanced memories have smaller critical charges.<sup>18</sup>

Armed with the concept of critical charge we will attempt to transit an ionizing particle through a device to see what occurs in the device material (see figures 8a thru 8c).

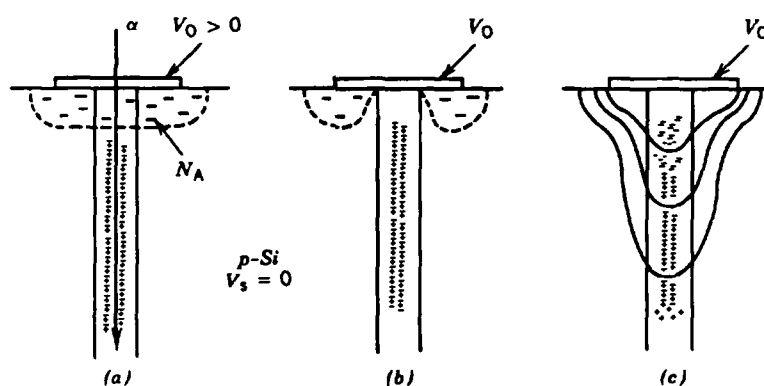


Figure 8. Response of a diode junction field to heavy ion penetration: (a) the ion penetrates and creates a column of electron-hole pairs; (b) the depletion layer collapses; (c) equipotential lines extend down the track.<sup>21</sup>

As the ionizing particle begins its transit it causes the formation of electron-hole pairs in its wake. The charge carriers diffuse and drift radially from the primary ionization

track, and dissipate energy by also ionizing the semiconductor material. If they are created in the depletion region surrounding a junction, the electron-hole pairs created by these secondary ionizations are rapidly separated and collected by a large internal electric field. Electrons or holes that are produced outside the depletion region can diffuse to the edge of the depletion region and be pulled into the node where logic information is stored, thus enhancing the process that can cause information loss.

The charge collected by drift results from charge deposited in the depletion region and charge which is collected from beyond that region by funnelling.<sup>55,56</sup> The funnel is an extension of the charge collection region by an extension of the electric field lines along the ion track. This particle-induced funnel causes a greater amount of the charge deposited by the ionizing particle to be collected promptly, around 300 picoseconds, thus increasing the likelihood of a SEU.<sup>19</sup> A more detailed look at this "funnel" concept follows.

### 2.1.3. The Funnel

The model most often used to describe the funnelling mechanism is the McLean-Oldham<sup>20</sup> effective funnel length model. This model assumes at first that the track of an ion can be thought of as an infinitely long uniform column of charge with an initial radius of 0.1 micrometer that is generated in 1 picosecond. This cylinder expands in the radial direction by ambipolar diffusion. This charge column endures until the plasma density drops to about the substrate doping density.

The creation of electron-hole pairs in the original depletion layer results in the neutralization of the depletion layer electric field, the collapse of the junction, and propagation of the electric field along the ion track into the previously neutral substrate. During the charge collection process, the depletion region electric field extends down the charge column. After the depletion layer is neutralized, we have a dense column of

charge, in reality a "plasma wire" in contact with an electrode, which tends to screen external electric fields from the interior of the column. The distortion of the equipotential lines down the track means that much more charge is rapidly collected outside the depletion region than would otherwise be possible. Thus funnelling will cause more charge to be collected at the struck node thus increasing the possibility of upset (figure 9).<sup>21</sup>

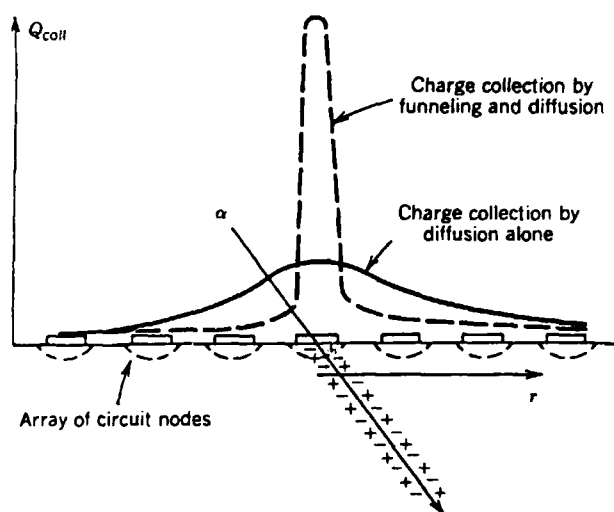


Figure 9. Charge collection curves for a circuit array showing that the maximum charge is collected at the struck node due to funnelling.<sup>21</sup>

At the characteristic time,  $\tau_c$ , determined by the dielectric relaxation time of the substrate, the electric field lines return to the original depletion layer configuration. Thus, the electric field varies both as a function of position and time. The effective funnel length model assumes that this complicated spatially and time variant field can be represented by an effective average electric field that exists for a duration  $\tau_c$ , and it provides a self consistent way to determine this average electric field. Such an

assumption ignores many of the details of the transient response of the device but has been shown to have good agreement with experimental results for DRAM.<sup>20</sup>

#### 2.1.4. Physical Analysis

Kreskovsky and Grubin<sup>22</sup> have conducted detailed analyses and model simulations of this charge collection process using the drift and diffusion equations for electrons in the substrate and the Boltzmann transport equation for electrons in the active layer of devices. The transient response following the strike by a single ionizing particle requires that the transport of electrons and holes generated in the device and the equipotential distortions be determined as functions of time. This is done by the solution of the continuity equations:

$$\frac{\delta N}{\delta t} = -\nabla \cdot (N \mu_N \nabla \psi) + \nabla \cdot D_N \nabla N + G - R$$

$$\frac{\delta P}{\delta t} = \nabla \cdot (P \mu_P \nabla \psi) + \nabla \cdot D_P \nabla P + G - R$$

and Poisson's equation

$$\epsilon \nabla^2 \psi = e(N - P - N_D + N_A)$$

where

N and P are the number densities of electrons and holes

$\psi$  is the electrostatic potential

$\mu$  is the mobility

D is carrier diffusivity

$\epsilon$  is the device material permittivity

e is the electron charge



$N_D, N_A$  are the doping concentrations (donors/acceptors)

$R$  is a recombination term

$G$  is the generation of carriers such that:

$$G = \frac{N_p(r)}{\tau_p} \exp[-t(r)/\tau_p]$$

where

$N_p(r)$  = concentration of particles generated in the track

$t(r)$  = time elapsed from when the radiation particle penetrates the device to a specific point along the track.

$\tau_p$  = time constant of thermalization ( $\sim 3\text{psec}$ )

Two processes contribute to the generation of carriers: impact ionization and generation due to the energy absorbed from the incident ionizing particle. Additionally, the generation terms are highly material and bombarding particle dependent.

Recombination is modeled as a combination of Shockley-Read-Hall and Auger<sup>23</sup> recombination:

$$R = \frac{NP - N_i^2}{\tau_p(N + N_i) + \tau_n(P + N_i)} + r(N + P)(NP - N_i^2),$$

where  $\tau_p$  and  $\tau_n$  are the carrier lifetimes (around  $1 \mu\text{sec}$ ) and  $r$  is the Auger rate constant. Note that the carrier lifetimes greatly exceed the lifetime of a SEU transient.<sup>22</sup> Arbitrary adjustments of the Auger rate constant has allowed reasonable matches between experimental work and computer simulations.

The above only prepares one to begin the considerations essential to model SEU simulations on a computer. However, it must be noted that present modeling tools restrict simulations to a two-dimensional analysis and therefore approximations have to

be made. The details of the approximations and the modeling processes themselves are beyond the scope of this research work and thus, suffice it to say, that the efforts to find truly predictive simulations of the SEU phenomena continue. However, the results of such work have led to some of the device protection methods that will be considered next.

#### 2.1.5. Methods of SEU Protection

As mentioned in the introduction section, alpha particles emitted in the header-package can be stopped from entering the chip by a simple passivation layer. Since the passivation layer technique does not stop all cosmic rays other techniques must be tried. As device miniaturization increased SEU susceptibility, the following process evolutions occurred: increasing doping concentrations, decreasing oxide thickness, and making twin and/or retrograde tubs on very thin epitaxial layers. These efforts attempted to reduce the charge collected from ion bombardments. The CMOS-on-epi technology placed the active regions of a device above a heavily doped substrate. The Silicon-on-Sapphire (SOS) technology sought to use an insulating substrate. The Silicon-on-insulator technology placed an insulator under the active devices. These modifications increase capacitances per unit area and reduce funnel collection of ionization generated charges.<sup>24</sup> The basic problem remains however, that heavy ions, such as oxygen and iron (normal constituents in the cosmic spectrum) can still generate sufficient charge in a circuit node to cause a logic state change. On a typical CMOS SRAM circuit, in a reasonable cosmic ray environment, approximately  $10^{-6}$  errors/bit/day will occur. A hit at the appropriate drain node deposits charge which drives the connected gate to the opposite bias. At this point, it is a race as the active transistor on the hit node tries to eliminate the deposited charge and restore the proper gate voltage before that charge switches the gate bias of the active transistor on the hit node. Frequently, as shown by the space environment

error rates, the race is lost. One solution for MOS logic circuits then, is to adjust the race by increasing the RC time constant of the coupling lines. The amount of RC adjustment is a function of the circuit parameters such as nodal capacitance. For a 16K SRAM, 100K ohms resistance in the feedback path (figure 6) has successfully prevented SEU for 140 Mev Kr at room temperature. This resistance is usually generated by high value polysilicon resistors. The increased resistance does increase the write time and thus SEU hardening impacts on performance.<sup>25</sup>

Recent developments at Sandia Labs have led to a new SRAM (the LRAM) that was developed from fundamental studies of SEU mechanisms. The resistors of a normal SEU hardened SRAM simply slow the response of the memory cell, allowing recovering from the transient. The LRAM (Figure 10) uses resistors for a essentially different

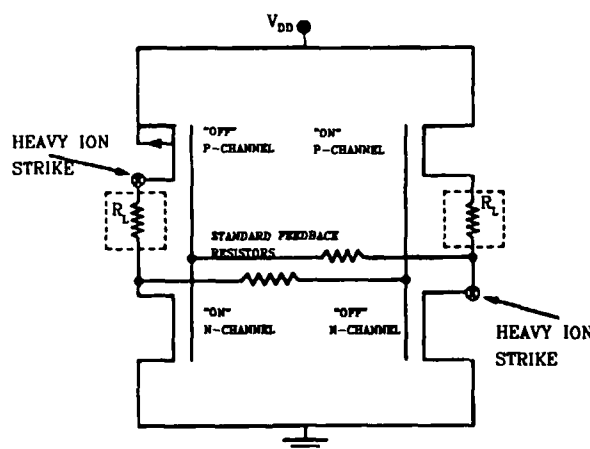


Figure 10. The LRAM design.

purpose. In addition to the normal feedback resistor, a second resistor, labeled  $R_L$  in Figure 10, is placed between the p-drain and information node of each inverter. This new resistor and the on n-channel transistor form a voltage divider at the storage node, allowing cell designs that limit the induced transient amplitude at this point to values below the switch point of the inverters. Consequently, a strike in the off p-drain can

not produce an SEU. The LRAM was created by adding only one additional mask level to the fabrication process. The LRAM uses resistors that are an order of magnitude smaller than those of the standard SEU hardened SRAM and has write times that are 50% of those of the standard SEU hardened SRAM. Subsequently, the LRAM provides a future for SEU hardening with increased device miniaturization that was not possible with just the resistive decoupling SRAM.<sup>26</sup> However, this technology has not yet been adopted by commercial device makers because of the difficulties involved in introducing this into their process lines.

## 2.2. Californium-252 and the Fission Process

Nuclei that fission provide the only natural source of energetic heavy ions with masses that exceed those of alpha particles. Spontaneous fission is only a useful source of heavy ions from transuranic isotopes with large mass numbers. Californium-252 is among the most widely used of such sources. Table 2 details some properties of <sup>252</sup>Cf that make it useful for this experiment:

CALIFORNIUM-252 FACTS	
Effective half-life:	2.65 yrs
Alpha decay half-life:	2.73 yrs
Spontaneous fission half-life:	85.5 yrs
Alpha particle energy:	6.117 Mev
Gamma emission rate:	$1.3 \times 10^7$ photons/s/ $\mu$ g
Specific activity:	approximately 500 $\mu$ Ci/ $\mu$ g
Average neutron energy:	2.35 Mev
Neutrons per fission:	3.76
Fission rate:	$6.2 \times 10^5$ /s/ $\mu$ g
<LET>=	44 Mev/(mg/cm <sup>2</sup> ) $\pm$ 7% (in Si)
after 5 microns of Si, <LET>=	32 Mev/(mg/cm <sup>2</sup> )

Table 2. Important Properties of <sup>252</sup>Cf.

Each fission results in two oppositely directed fission fragments. The spontaneous fission process is asymmetric and thus the fission fragments masses form into "heavy" and "light" fragment groups.<sup>27</sup> Figure 11 shows the fragment mass distribution and the average single fragment kinetic energy for  $^{252}\text{Cf}$  fission fragments. The pre-neutron-emission fission yield is marked as  $N(m^*)$  in Figure 11, the unmarked mass curve represents the post-neutron-emission yield.

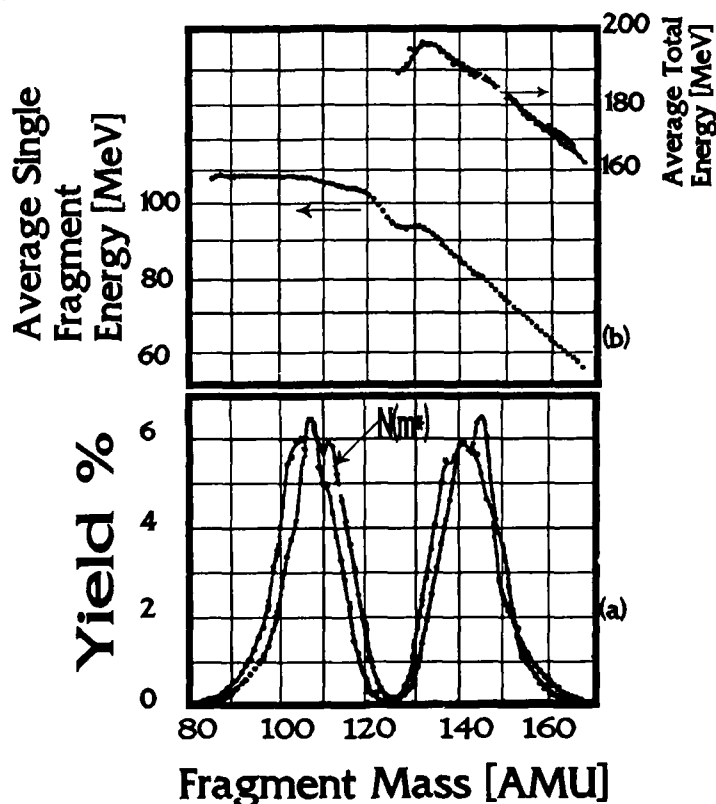


Figure 11. Mass and energy distributions for the spontaneous fission of  $^{252}\text{Cf}$ . (a) the mass distributions as a function of fragment mass,  $N(m^*)$  marks the pre-neutron-emission mass distribution, the post-emission mass distribution is unmarked. (b) the average single-fragment and total pre-neutron-emission kinetic energy as functions of mass.<sup>28</sup>

Note that the heavy-fragment peak is around 142 atomic mass units (AMU) while the light-fragment peak is around 108 AMU. In looking at the energy distribution note that the lighter fragment has more kinetic energy and its value is more nearly constant. The heavy fragment mass kinetic energy rapidly decreases with increasing mass.

Figure 12 is a pictorial attempt to help explain the asymmetry of spontaneous fission. Based on the liquid drop model there is no prediction of the observed asymmetry of fission.

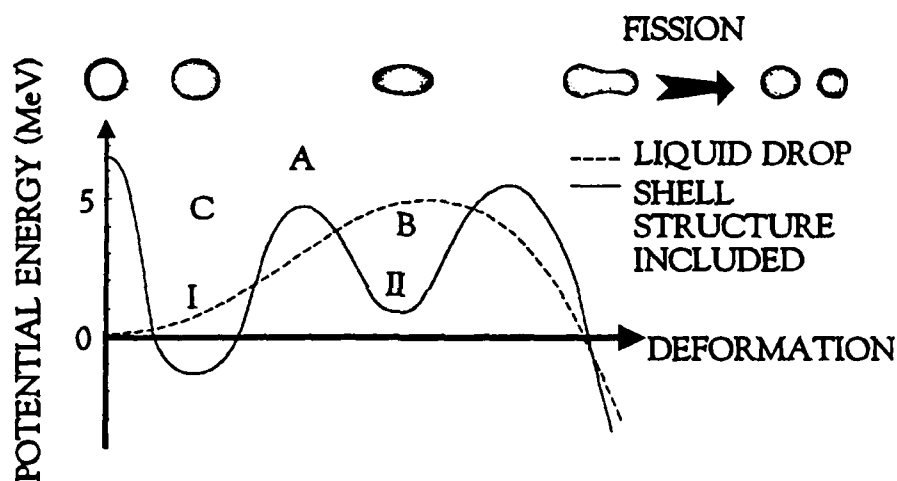


Figure 12. Potential energy function for deformations leading to fission.<sup>29</sup>

First it is important to note that asymmetric shapes have lower potential energy than symmetric shapes. Thus asymmetric fission is favored for nuclei with low excess energy. The Coulomb energy would be minimized if the fission evenly divided the number of protons but this generally does not occur because shell closings favor magic numbers. The fragments tend to have the number of protons and the number of neutrons each around the magic numbers of 50 and 82; it is assumed that this is energetically favorable<sup>30</sup> for a system seeking the lowest potential energy level and consequently the

highest binding energy per nucleon. The elongated nucleus shapes at the first (I) and second (II) minima correspond to those for the ground states for nuclei with those shape isomers in the region of uranium. The double humped barrier, which includes the shell effects, results in three types of fission:

(1) from states A in the area above the threshold, with decays on the order of  $10^{-16}$  to  $10^{-20}$  seconds.

(2) from states B where only the second barrier peak plays a role. These have decay times of  $10^{-2}$  to  $10^{-9}$  seconds.

(3) Finally, spontaneous fission from states C is a very slow process, held in abeyance by both humps of the barrier. Here half-lives range from hours to  $10^9$  years or more.<sup>29</sup> This is the type of fission that typifies the process for  $^{252}\text{Cf}$ .

Table 3 provides the mean values for the fission fragments for energy and mass according to the fragment groupings "heavy" and "light."

	Energy (MeV)	$\sigma_{\text{ENERGY}}$	MASS (AMU)	$\sigma_{\text{MASS}}$
Light	$103.77 \pm 0.5$	5.48	106	6.53
Heavy	$79.37 \pm .5$	8.23	141.9	6.55

Table 3. Mean values of energy and mass for  $^{252}\text{Cf}$  fission fragments.<sup>31</sup>

The fragments initially have net positive effective charges as large as +18 or +20 electronic charges. Interactions with matter result in electrons being attracted to these positive ions and thus the positive effective charge is reduced.<sup>27</sup>

### 2.3. TFD Scintillation Theory

Thin films of plastic scintillator material are used as heavy ion transmission detectors which respond to the energy lost by a particle as it travels through the

detector. The greatest advantage that such detectors provide is that they can be made as thin as  $20 \mu\text{g}/\text{cm}^2$  and thus are between one or two orders of magnitude thinner than is possible with other solid state particle detectors. Thus thin film scintillators can be used to determine the energy of transiting particles while the particle loses only a small percentage of its initial energy. Understanding the response of these films has been the subject of research by several groups and remains a subject for further investigation. Knoll best summarizes the current understanding of this scintillation process by stating,

“...the response of these films does not follow directly from the expected energy loss of ions in the detector, and appears to be a more complex function of the ion velocity and atomic number. The light yield per unit energy loss increases with decreasing atomic number of the ion, so that thin films can be useful transmission detectors for protons and alpha particles even when the energy deposited is relatively small.”<sup>27</sup>

Muga<sup>32</sup> first reported a technique for using a thin film detector to record an output pulse responding to the energy loss of the  $^{252}\text{Cf}$  fission fragments traversing the film. He indicated that there was about a 3.5% fission fragment energy loss per  $100 \mu\text{g}/\text{cm}^2$  scintillator thickness and reported a clear separation between the light and heavy fragment TFD signal spectra. Figure 13 shows a contour plot of Muga's correlated two parameter experiment that compared TFD scintillator response with that of a heavy-ion detector that measured the  $^{252}\text{Cf}$  fission fragment energy after the passage through the scintillator.



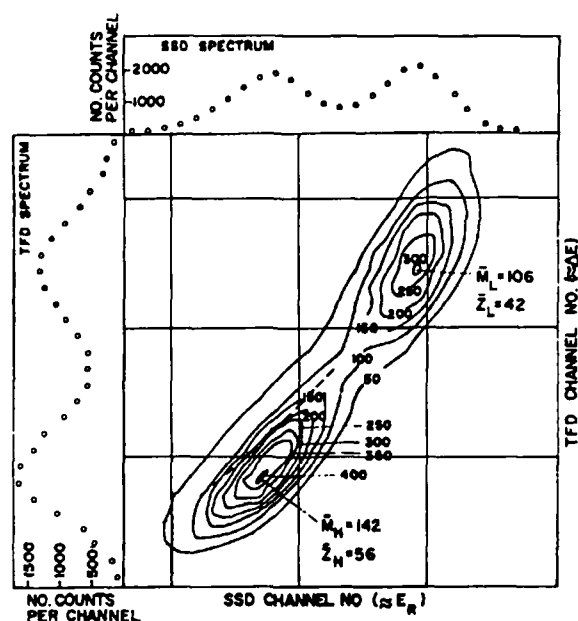


Figure 13. Contour plot of a correlated two parameter experiment<sup>32</sup> on  $^{252}\text{Cf}$ . Inserts show the summed spectra, over TFD and solid state detector contours, respectively.

Generally, it is clear that the more energetic light fission fragment creates a larger TFD signal than the more massive heavy fragment. Additionally within each grouping, heavy or light, the more energetic fragments produce larger responses. The overall shape of the TFD spectrum seems to mirror that of the solid state detector residual kinetic energy spectrum except that the heavier fragment part seems to peak higher and have less width for its TFD response. Muga determined that TFD response was shown to depend predominantly on the velocity and atomic number of the transiting ion for heavy ions.<sup>33</sup> Figure 14 shows a plot of average fragment velocity versus TFD channel number that Muga<sup>32</sup> obtained in working with degraded beams of  $^{252}\text{Cf}$ . Pulse height distributions of the TFD were obtained and the heavy and light fragment peak positions were plotted as a function of average velocity of the passing fragments.

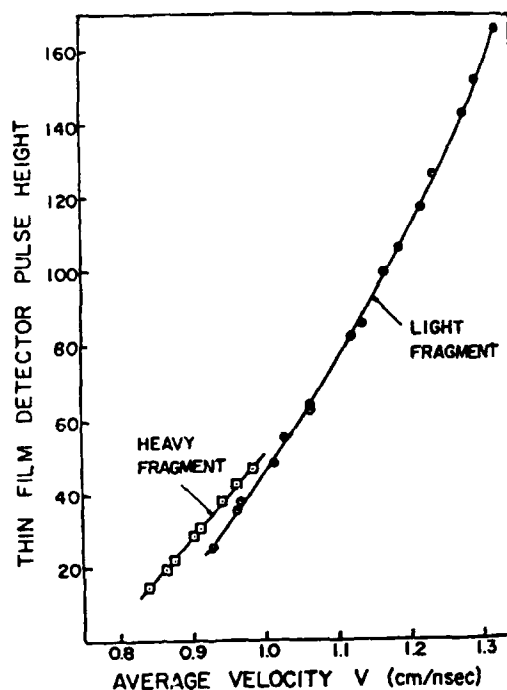


Figure 14. TFD response to degraded fission fragments showing pulse height distribution as a function of average fragment velocity.<sup>32</sup>

In analyzing the TFD response for fission fragments, McDonald et al.<sup>34</sup> suggested that because of the high track density, and subsequent recombination in the case of heavy ions, TFD response would be roughly proportional to just velocity. This differed from Muga and Griffith's<sup>33</sup> result with light ions such as  $^1\text{H}$  and  $^4\text{He}$ , but McDonald et al. offered figure 14 (Muga's fission fragment work) as evidence showing that TFD response was almost a linear function of the average velocity of the fragment and thus basically independent of its mass. McDonald et al. concluded that this simple velocity dependence could only be obtained for heavy ions.

The work of N. N. Ajitanand and K. N. Iyengar<sup>35</sup> resulted in an improved method of scintillator production which resulted in better separation of the heavy and

light fission fragment groups and a manufacturing technique that was simpler. Additionally, their work showed that the fission fragment response showed a saturation of response with respect to energy loss in the scintillator. Figure 15 shows that for heavy ion energies below 0.5 MeV per nucleon TFD response saturates.

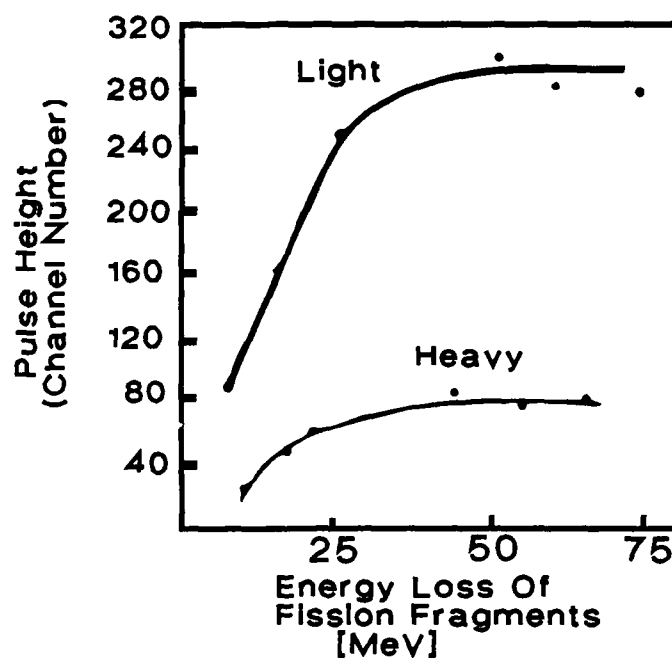


Figure 15. The relative light and heavy fragment peak pulse heights as a function of the fragment energy loss in the thin film scintillator.<sup>35</sup>

These investigations led to theories on the response of TFD by Muga et al.<sup>32</sup> and Ajitanand<sup>35</sup> but both required fitting parameters that explained their data at 100  $\mu\text{g}/\text{cm}^2$  thickness, but failed to address scintillators of a different thickness. Kanno and Nakagome<sup>36</sup> have published a new model of TFD response that has been shown to be accurate for thin scintillators up to 300  $\mu\text{g}/\text{cm}^2$ . Additionally, this model has explained

the light ion data of Muga and has accurately modeled the response for  $^{252}\text{Cf}$  transiting through scintillator thicknesses of 50 to 300  $\mu\text{g}/\text{cm}^2$ .

Following a brief overview of this new luminescence model we will investigate each step of the model's light yielding scheme and examine the results obtained with  $^{252}\text{Cf}$ . Basically, Kanno and Nakagome model the luminescence yield as a three step process:

- (a) the heavy ion entering the scintillator causes free electrons to recoil.
- (b) the recoiling free electrons excite the  $\pi$ -electrons of the organic molecule.
- (c) as the  $\pi$ -electrons return to their ground state configuration photons are emitted.

To produce the recoiling primary electrons one considers that the heavy ion causes the electrons to recoil by the Rutherford scattering cross section  $d\sigma$ ,

$$d\sigma = \frac{1}{4} \left[ \frac{e^2 Z_{\text{eff}}}{\mu V^2} \right]^2 \frac{1}{\sin^4(\theta/2)} d\theta$$

where:

$V$  = the velocity of the heavy ion.

$$Z_{\text{eff}} = \text{the effective charge of the heavy ion} = Z \left[ 1 - \exp \left( \frac{-125 \beta}{Z^{\frac{2}{3}}} \right) \right]$$

where:

$\beta$  is the ratio the velocity of the heavy ion to the speed of light.

The recoiled electron leaves at an angle  $\Theta$  with energy  $E_e = \frac{4mE}{kM} \cos^2\Theta$ , where  $k$  is the conversion factor from MKS units to cm, AMU, ns and MeV in energy ( $k=1.0365$ ). The range of the primary electron is:

$$R = 9.62 \times 10^{-3} \left[ \frac{\text{cm}}{\text{MeV}} \right] \frac{4mE}{kM} \cos^2 \Theta.$$

These recoiled electrons move from their original position,  $x$ , to the limit of their range as show in Figure 16(a) below.  $R_0$  is determined by substituting  $\Theta=0$  degrees in the range equation above. The accessible area of recoil as designated in Figure 16(a) is defined by Kanno and Nakagome as region  $P(R_0, x)$ .

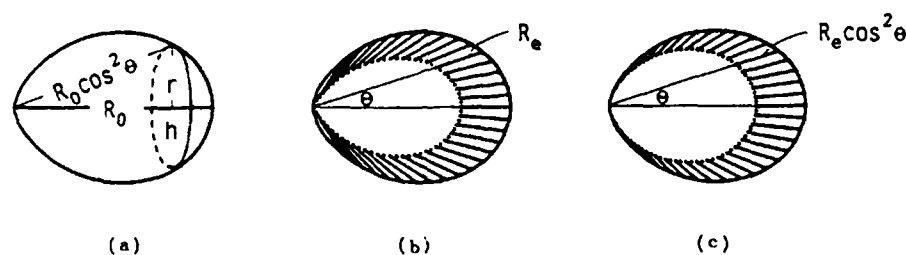


Figure 16. A pictorial view of the recoil region,  $P(R_0, x)$ , available to the recoiled primary electrons. (a) The entire region of travel available to the recoil electrons. (b) The hatched region shows the area where  $\pi$ -electrons are excited. (c) Actual area calculated for ease of calculations,  $P_{\text{eff}}(R_0, x) = P(R_0, x) - P(R_0 - R_e, x)$ .

Key in knowing the final luminescence value is the number of  $\pi$ -electrons that are excited. This calculation is quite involved even after the following assumptions are made to simplify the process:

- (1) The recoil electrons are assumed to transfer a constant amount of energy to the  $\pi$ -electrons which are assumed to be equally spaced throughout the scintillator.
- (2) The scattered primary electrons move in the direction of recoil and the number of electrons scattered by the primary electrons is ignorable.

(3) In the initial portion of their travel the primary recoil electrons are traveling too fast to excite the  $\pi$ -electrons. Only in the hatched region of Figure 16(b) can  $\pi$ -electron excitation occur.

(4) For ease of calculation we define and calculate  $P_{\text{eff}}(R_0, x)$  instead of the actual volume of the cross hatched area for Figure 16(b). The actual area calculated is depicted in Figure 16(c), where  $P_{\text{eff}}(R_0, x) = P(R_0, x) - P(R_0 - R_e, x)$ .

(5) The total number of  $\pi$ -electrons excited will be the integral of the product of  $d\sigma$  and  $P_{\text{eff}}(R_0, x)$ .

Since the scintillator is of a finite thickness,  $T$ ,  $P_{\text{eff}}(R_0, x)$  could fall outside of the scintillator. This significantly complicates the calculation of the effective region, the details of this calculation can be found in the original paper by Kanno and Nakagome.<sup>36</sup>

The total number of emitted photons is proportional to the integral of the  $\pi$ -electron density,  $\rho$ , the primary electron recoil cross section,  $\sigma$ , and the effective volume,  $P_{\text{eff}}(R_0, x)$ , along the ion path and can be calculated by: 
$$L = \int_0^T \rho \sigma P_{\text{eff}}(R_0, x) dx$$

where  $\rho$  is the density of  $\pi$ -electrons in the scintillator,  $T$  is the scintillator thickness,  $\sigma$  is the recoiling cross section of an electron and  $P_{\text{eff}}(R_0, x)$  is the effective volume along the path,  $x$ , of the heavy ion. Instead of integrating, Kanno and Nakagome, divided the scintillator into one hundred parts and summed  $L$  over the entire scintillator.

This model successfully predicted the photon production for a single ion species and accurately matched the empirical work of previous investigators. The calculation of the photon production for  $^{252}\text{Cf}$  bombarding a scintillator is a more tedious process that requires the superposition of yields produced by all the heavy ions with mass  $M$ , atomic number  $Z$  and kinetic energy  $E$  that represent the entire fission fragment spectrum. Figure 17 shows the calculated and experimental pulse height spectra obtained by Kanno

and Nakagome<sup>37</sup> for  $^{252}\text{Cf}$  bombarding scintillators of varying thickness. Each graph shows the calculated and experimental pulse height spectra of TFD for various film thicknesses. The solid smooth lines represent the calculated results while the histograms represent the experimental data from the scintillators. It is clear that the pulse height spectrum is satisfactorily represented by this model.

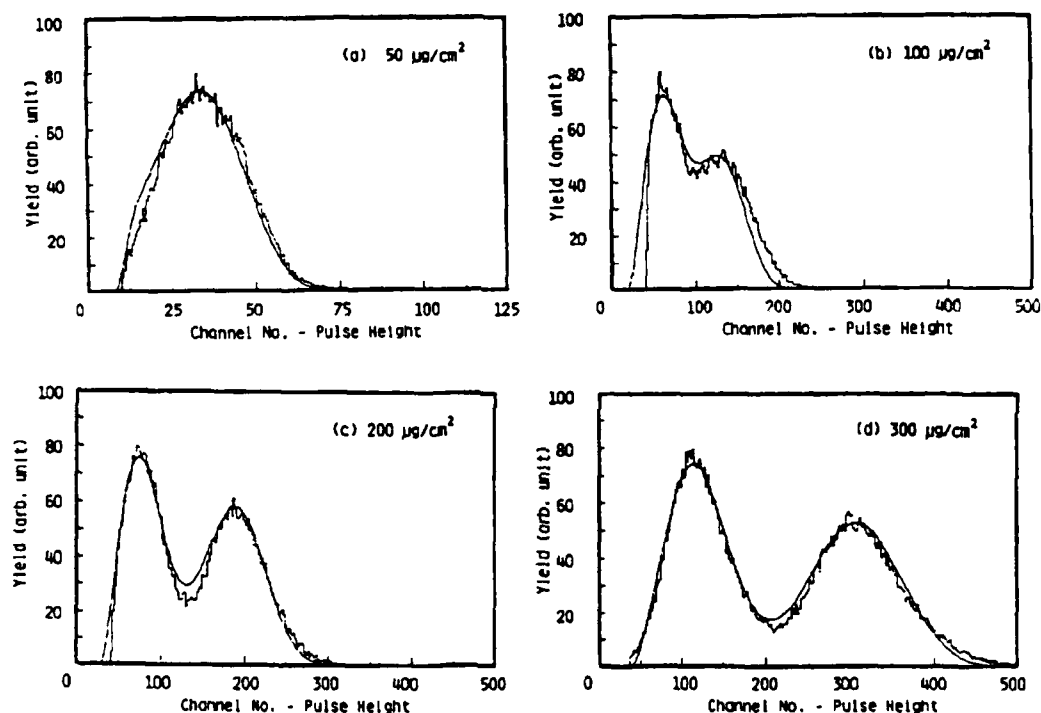


Figure 17. The calculated and experimental pulse height spectra of TFD for various film thicknesses. The solid lines are the calculated results while the histograms represent the experimental data from the scintillators.<sup>37</sup>

This investigation of scintillation theory has looked at empirical work and a relatively new theoretical model that accurately predicts scintillator response. In summary it is best to state that empirical and theoretical work support the contention

that the response of TFD does not follow directly from the expected energy loss of ions in the detector, but rather the luminescence yield is a complex but calculable function of the ion velocity, TFD thickness, and atomic number.

#### 2.4. Stopping Power And Fission Fragments

The energy loss of fission fragments in a medium is determined by electronic and nuclear stopping. Electronic stopping is defined as the energy loss to electrons through Coulombic interactions and this process is analyzed as an inelastic collision. Nuclear stopping is characterized by an elastic energy loss process that results from the energy loss due to collisions with the positive nuclear core. For energetic light ions, such as alpha particles, Bohr concluded that electronic stopping would dominate.<sup>38</sup> Fission fragments, however, present a more difficult problem to analyze because they are really partially stripped heavy ions with energies around 1 MeV/AMU and one must consider both electronic and nuclear stopping. Fission fragments initially carry with them only about one-half of their normal complement of electrons.

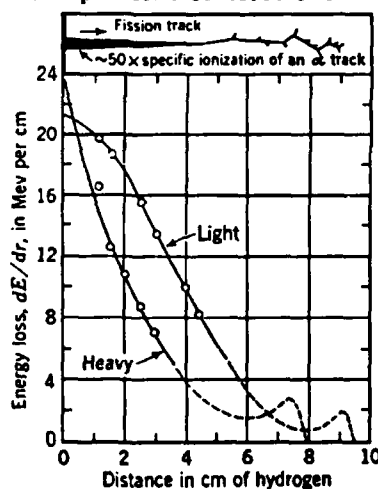


Figure 18. Energy loss per unit path length for fission fragments.<sup>39</sup>



Figure 18 shows the energy loss per unit path length for the average heavy and light fission fragment with an insert to show a schematic representation of a typical fission fragment track in a cloud chamber. Note that the energy loss per unit path length is the greatest at the beginning of the track and that, as verified by cloud chamber photographs, the final portion of the range is characterized by elastic nuclear collisions. The plateau region is where the transition from electronic stopping dominance to nuclear stopping occurs.

Lindhard et al.<sup>40</sup> developed the first unified approach to stopping and range theory that addressed both light ion and heavy ion (fission fragment) stopping. They showed that the interplay of electronic or nuclear stopping depends on velocity and the average charge,  $Z_1$ , of the particle. When the velocity is greater than  $\frac{2\pi e^2}{h} Z_1^{2/3}$  the stopping is describe adequately by Bethe's theory of stopping.<sup>27</sup> When the velocity is less than  $\frac{2\pi e^2}{h} Z_1^{2/3}$  nuclear stopping becomes important and must also be considered.

Forcinal et al.<sup>41</sup> demonstrated the relative importance of the relationship between nuclear and electronic stopping as shown in Figure 19. The graph is presented in Lindhard's terminology with the impinging ion energy,  $E$ , replaced with  $\varepsilon$  and the range,  $R$ , replaced with  $\rho$ , defined as:

$$\varepsilon = \frac{aM_{\text{target}}E}{Z_{\text{ion}}Z_{\text{target}}e^2(M_{\text{ion}} + M_{\text{target}})} \text{ and } \rho = 4\pi a^2 \frac{M_{\text{ion}}M_{\text{target}}N}{(M_{\text{ion}} + M_{\text{target}})^2}R,$$

where:

$$a = \frac{0.8853 a_0}{\sqrt{(Z_{\text{ion}}^{2/3} + Z_{\text{target}}^{2/3})}} \text{ and } a_0 \text{ is the Bohr radius, and } N \text{ is the target number}$$

density.

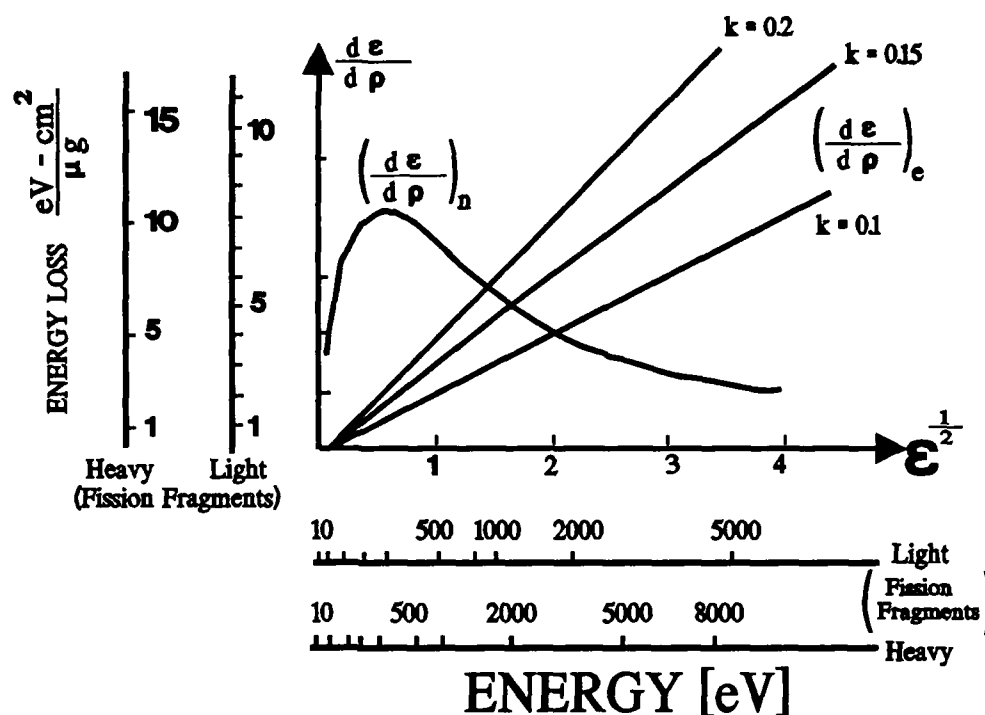


Figure 19. Nuclear and electronic energy losses in Lindhard's dimensionless units.<sup>41</sup> Actual values of  $dE/dR$  and energy are indicated for fission fragments bombarding silicon.

The curves representing the electronic  $(d\epsilon/d\rho)_e$  and nuclear  $(d\epsilon/d\rho)_n$  specific energy for fission fragments are drawn with axes corresponding to the actual values of the energy and of the specific energy loss for fission fragments striking silicon. The electronic stopping,  $(d\epsilon/d\rho)_e = k\epsilon^{-5}$  where  $k$  is a constant that depends on  $Z_{\text{ion}}$ ,  $Z_{\text{target}}$ ,  $A_{\text{ion}}$  and  $A_{\text{target}}$ , and is around 0.10 to 0.20.

Lindhard's theory allowed for the calculation of ranges to within a factor of two or three. Ziegler et al.<sup>38</sup> have compiled a large library of data on the penetration of energetic ions in solids and have produced a computer program called "The TRansport of Ions in Matter" (TRIM) to calculate the details of penetration for ions of any atomic number at energies up to 2 GeV/AMU. Ziegler's work now allows for an accuracy of

2% to 10% for stopping power calculations. The cited reference explains the physics of the calculations in a tutorial manner and presents source code for the TRIM program.

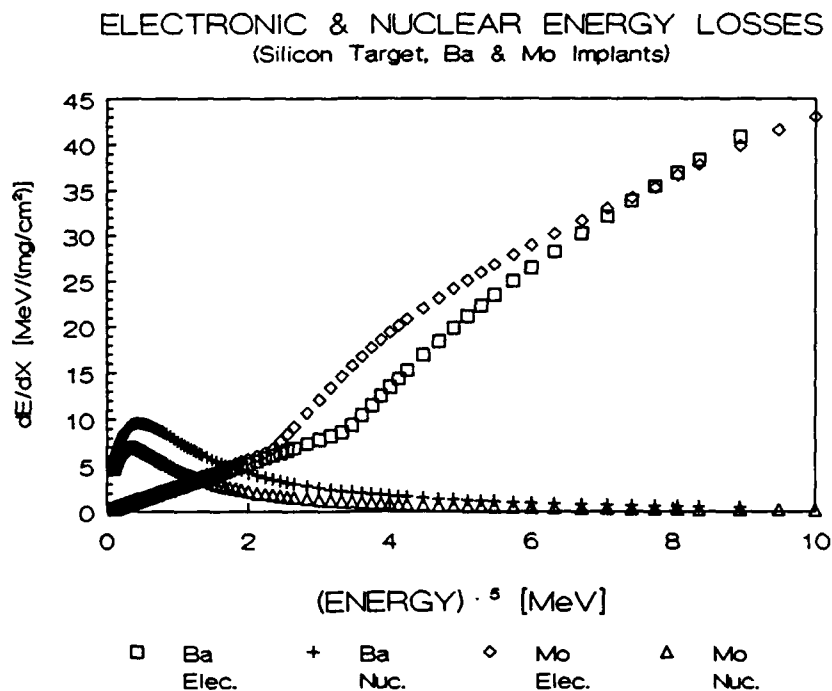


Figure 20. Electronic and nuclear stopping as determined from the computer code TRIM. Here Ba and Mo represent the typical heavy and light fission fragments bombarding silicon.

Figure 20 is a plot of the results obtained with TRIM when comparing the nuclear and electronic stopping when barium and molybdenum were used to represent the typical heavy and light fission fragments impinging on silicon. This look at the relationship between electric and nuclear stopping gives clear evidence that, in general, electronic stopping is the dominant mechanism in the scintillators and attenuators used in this experiment. However, both electric and nuclear stopping play a significant role in the electronic devices under test.

## CHAPTER 3

### MATERIALS AND APPARATUS

#### 3.1. The Test Chamber

The test chamber is basically a modular three-part vacuum chamber with electrical and mechanical feed throughs. The chamber sections are designed with flange faces and o-ring gaskets that allow for the addition of new modules. Figure 21 is a photograph of the SEU chamber. Close-ups of the interior of each section are shown on the next few pages. Figure 4, in the introduction section, provides a schematic setup of the chamber that greatly aides in following the chamber component discussion below.

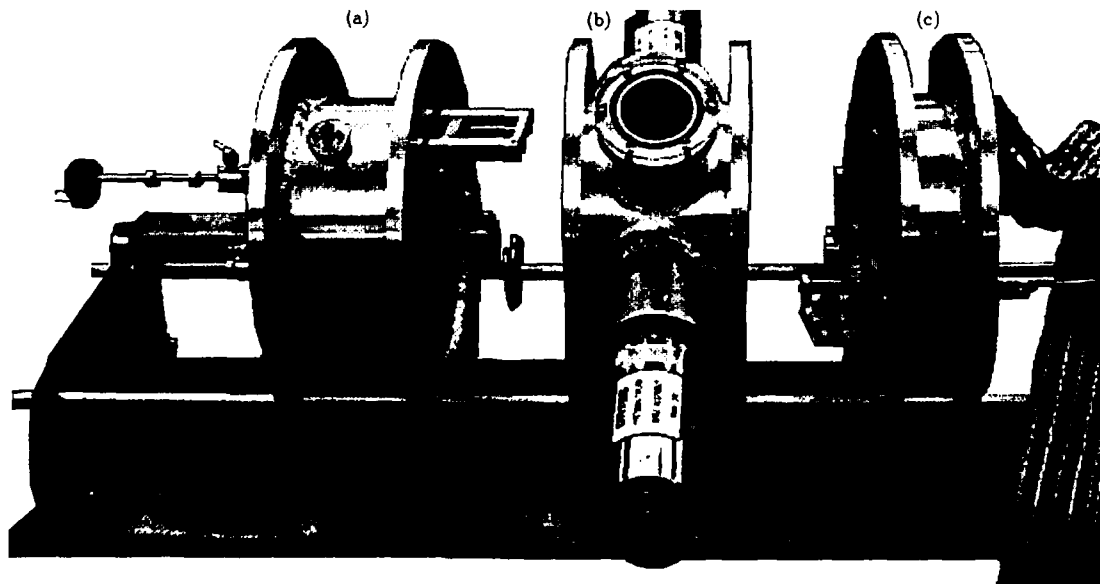


Figure 21. The SEU tester vacuum chamber.

The chamber section marked as (a) in Figure 21 contains the source holder, the movement control rods for positioning the fission fragment source, and a beam blocking wheel. Figure 22 provides a close up of the interior of this section. The beam blocking wheel can be replaced with a wheel of attenuators in order to lower the fragment LET.



Figure 22. A close-up of the source holding section. Push-pull rods allow the source to be moved from the exterior while the chamber is under vacuum. The blocking wheel shown can be replaced with a wheel of attenuators.

A  $0.75 \mu\text{C } ^{252}\text{Cf}$  source, not shown, is used to provide fission fragments. The source consists of a 5 mm diameter spot of electro-deposited californium oxide centered on a 0.5 inch diameter platinum foil that is 0.005 inches thick. To avert flaking, the californium is fixed to the supporting foil by diffusion bonding at 1000 °C. The source is covered with  $50 \mu\text{g}/\text{cm}^2$  of gold to preclude loss of the californium by recoil. Such a source is commercially available from Isotope Products Laboratories of Burbank, CA.<sup>42</sup>

The center section, marked as (b) in Figure 21 contains a view port, an iris, the light pipes, and the scintillator film mounting apparatus. The view port is used during initial system alignment. Great care is exercised to insure that the view port is closed during normal operations in order to prevent damage to the photomultiplier tubes. The iris is available to reduce the fission fragment beam size or to aid collimation of the beam.

Figure 23 is a close-up of the center section. The iris has been removed for this photograph to make it easier to see the light pipes. The light pipes are made of Lucite and are optically mounted to the faces of RCA 8575 photomultiplier tubes placed outside the vacuum chamber. The light pipes are symmetrically placed on either side of the scintillator ring. The concave ends of the pipes facing the scintillator are hemispheric with the center of curvature being coincident with the center of the scintillator ring. This geometry was selected in an effort to maximize the capture of the small amount of scintillation light. The fission fragment enters the light collection system through a 6mm diameter hole, passes through the scintillator, and exits through another 6mm opening and continues its flight toward the DUT. The scintillator film serves as a transmission detector which responds to the small amount of energy deposited by the particle as it passes through the film.

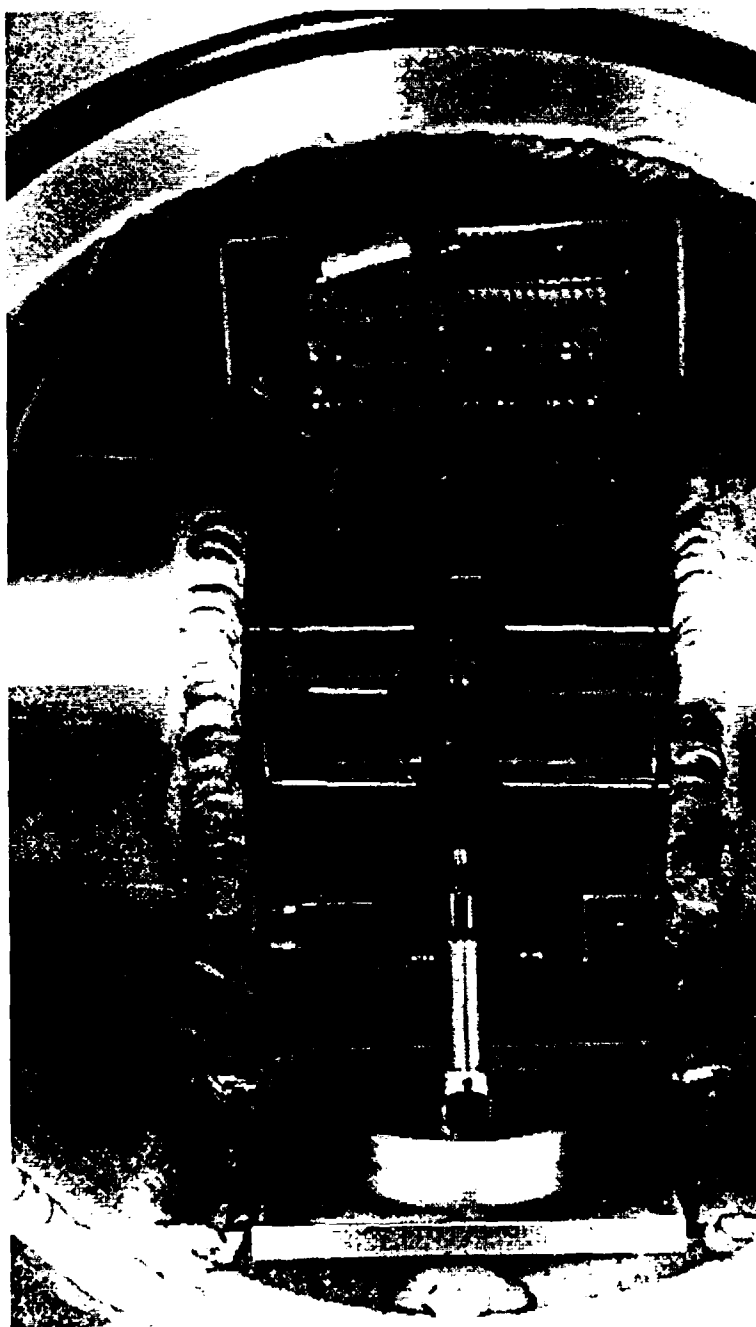


Figure 23. A close-up of the chamber center section. This view is taken from the source location and shows that a fission fragment would pass through the light pipe openings, through the scintillator, and then onto the DUT.

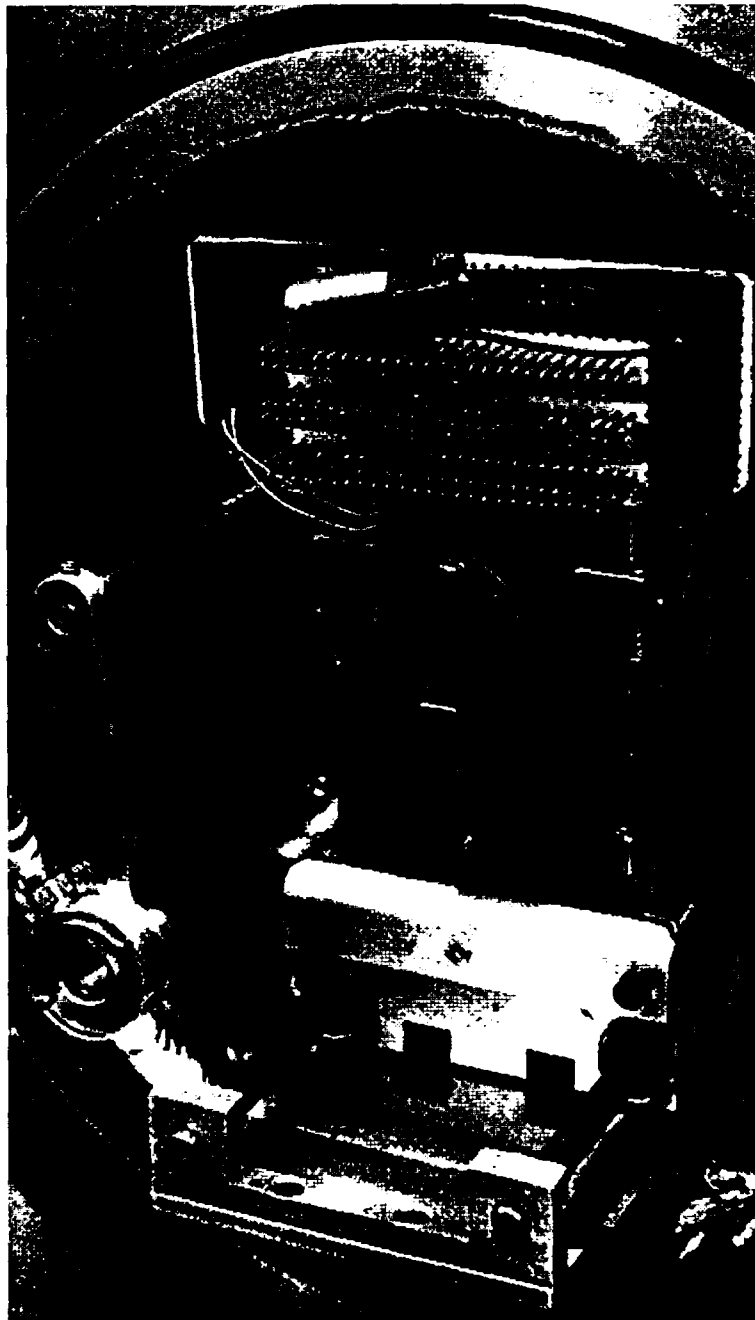


Figure 24. A close-up of the DUT card and surface barrier detector.

The section marked (c) in Figure 21 contains the solid state detector, the DUT mounting card, the DUT, electrical wiring to the external memory tester, and motion



control rods for the solid state detector and the DUT card. Figure 24 shows a close-up of the DUT card and the SBD. The solid state detector in use is an ORTEC heavy-ion surface barrier detector (SBD) with a 60 micron depletion depth. This detector is used to calibrate the scintillators to insure that the scintillator response accurately depicts the californium spectrum. Additionally this SBD is used to measure the flux incident upon the DUT and the thickness of the scintillators and attenuators. During actual upset measurements the SBD is moved out of the fission fragment beam to allow the DUT to receive the fragment flux. The DUT is the particular memory chip that is tested and is electrically wired to the memory tester outside the chamber that continuously exercises the chip during a test. The electrical feed through that passes through the vacuum wall consists of 150 wires in order to insure support for a wide variety of testing configurations.

This vacuum chamber, however, simply provides the environment for SEU to occur. The ability to determine when an SEU occurs and which fission fragment is responsible requires the use of instrumentation that is external to the vacuum chamber. The details of this instrumentation will be discussed in the section on data collection electronics.

### 3.2.Data Collection Electronics

#### 3.2.1. Nuclear electronics

The electronics setup that processes the signals from the test chamber and enables the upset data and the fission fragment energy that caused the error to be collected into the computer is shown in Figure 25.

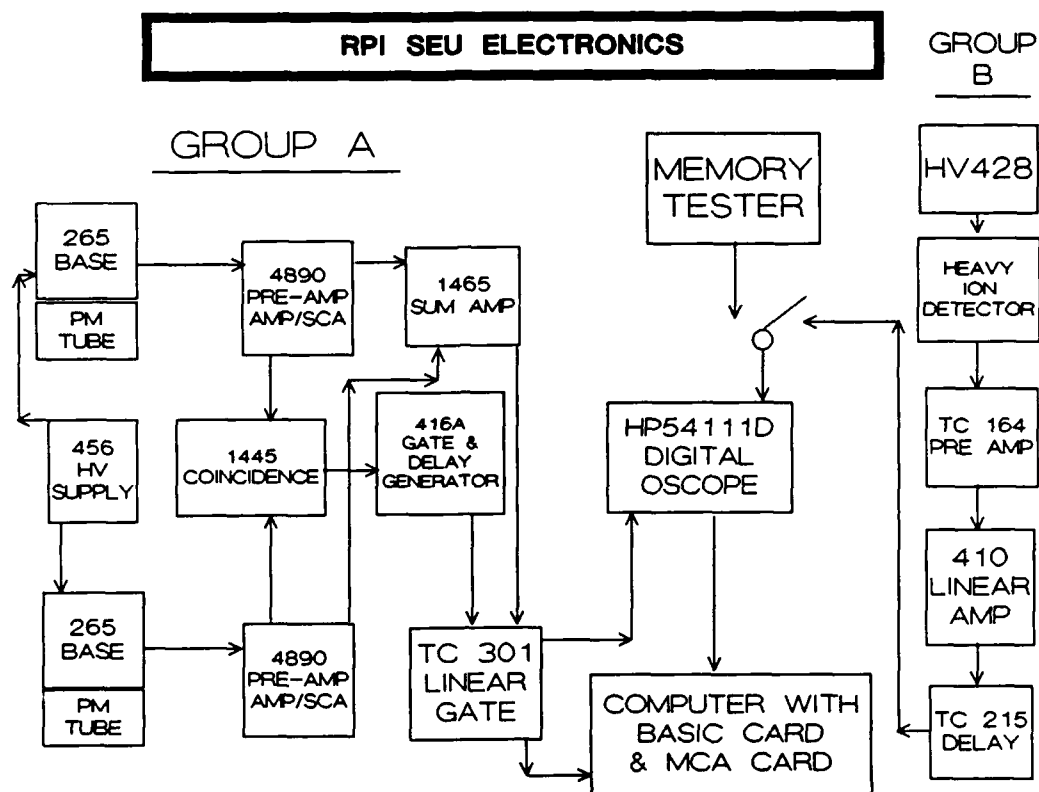


Figure 25. Electronic Equipment For the SEU System.

The equipment labeled as "Group A" produces the scintillation voltage signal that identifies each individual heavy ion. The equipment in "Group B" allows the use of a standard heavy ion surface barrier detector to calibrate the scintillator response against the  $^{252}\text{Cf}$  spectrum. The HP54111D digital scope is used with either "Group A" and "Group B" to calibrate the system, or with "Group A" and the memory tester to measure the DUT upset cross section.

Our tests are all run by exercising the memory while it is bombarded. Basically a pattern (logical 1 or 0) is written throughout the memory, then the tester checks each location to see if any errors have occurred. Errors are sent to a counter and collected along with the scintillation pulse height by the microcomputer controlling the experiment

while the computer simultaneously collects scintillation pulse height information into a pulse-height multichannel analyzer (MCA) card.

### 3.2.2. Memory Tester

The memory tester used throughout this experiment was provided by the Jet Propulsion Laboratories (JPL) of the California Institute of Technology. This memory tester is a "one-of-a-kind" laboratory-built apparatus and is not commercially available. JPL previously used this memory tester for SEU work at accelerator facilities.

By design, this tester's primary function is to provide the user a count of the total number errors encountered since it began checking the DUT. The number of cumulative errors is displayed by a counter. The user may reset the counter to zero and begin the testing cycle anew by pressing a button labeled "reset."

The test pattern, DUT chip cycling, and tester operations are governed by hexadecimal codes in erasable programmable read-only memory (EPROM) which begin operations and testing when the tester is turned on. The EPROM can be erased by use of an ultra-violet light and then programmed again if a different testing pattern is desired. Throughout these SEU experiments a checkerboard pattern consisting of ones alternating with zeroes was used.

The JPL tester executes memory testing by dividing the DUT storage locations into two equal regions, and writing the same pattern into each region. As the tester cycles through each individual memory location it:

- 1) reads the information stored in that location.
- 2) compares the information found with what should be stored there.
- 3) increments the display counter if an error is detected.
- 4) rewrites the location with the appropriate one or zero, as determined by the EPROM, and moves on to the next memory location.

### 3.2.3. Interface

Because the JPL memory tester was designed to merely display a count of the total cumulative errors, modifications were necessary in order that each error could be associated with the scintillator pulse height information for the fission fragment that caused the error. Since the JPL tester did not come with detailed schematics, and would have to eventually be returned, internal modifications were ruled out. However, the JPL test configuration allowed for the building of interfacing circuitry, external to the tester, electrically placed between the tester and the DUT. Therefore an interface was built to communicate each error, as it occurred, to an external controller. The basic operation of the interface follows:

- 1) each error sets a latch in the interface. When prompted by an external high (5 volt) logic pulse, a logic high is released if an error was stored; a logic low (zero volts) is released if no error information is present.
- 2) as each fission fragment is detected by the Group A electronics of Figure 25 the delay and gate generator sends a logic pulse to the linear gate to release the pulse height information. This same logic pulse is sent to the interface to release the information on whether or not an error occurred.
- 3) the released pulse height information and the error information (high or low) are sent to the digitizing oscilloscope as shown in Figure 25.

Thus the interface provides the means for an external controller to collect error information from the memory tester and marry it with pulse height information from the nuclear electronics. Details of the data collection scheme will be discussed in the section on data collection and the microcomputer.

#### 3.2.4. Data Collection And The Microcomputer

The data collection is controlled by a Hewlett Packard microcomputer (model PC-308) of the IBM AT class. The program that performs the data collection is in the appendix. The data collection scheme is simple and is outlined below:

- 1) the computer orders the digitizing oscilloscope to reset and await a triggering signal from the delay and gate generator.
- 2) when a fission fragment transits the scintillator foil and is processed by the nuclear instrumentation, the delay and gate generator logic signal is sent to the digitizing scope. This same logic signal releases the pulse height information and error information. The pulse height information appears on channel 1 of the digitizing scope and the error information appears on channel 2.
- 3) the digitized data are sent to the computer, stored in a matrix, and the process begins again.

Currently, the program collects 16000 data pairs in each file. Data pairs consist of the scintillation pulse height voltage (0 to 10 volts) and error information (0 volts for no error, 5 volts for an error). In order to develop the upset cross sections essential to SEU investigations this raw data must be analyzed. Data analysis will be discussed in the section on methods of determining SEU cross sections.

#### 3.3. Thin Film Scintillator Preparation

A thin film scintillator with good ability to resolve the fission fragment groups is made by dissolving Nuclear Enterprises NE-191 plastic scintillator micro-spheres in toluene and allowing several drops of the solution to dry under somewhat prescribed conditions. It was determined that mixing 0.56 grams of NE-191 powder in 50 ml of toluene would produce a thin film scintillator of around  $250 \mu\text{g}/\text{cm}^2$  thickness. Varying

the amount of NE-191 powder per 50 ml solution of toluene will increase or decrease scintillator thickness proportionally. Film thickness is measured with the surface barrier detector by the alpha peak shift using the 6.119 MeV alpha peak for  $^{252}\text{Cf}$ ; details of the thickness measurements will be discussed in the procedure section.

Scintillation production should begin by soaping a glass plate with a water soluble soap solution and letting this dry. This pre-treatment will aid in removing the finished scintillator from the glass. Several drops of the NE-191 and toluene mixture should be dropped from around a 1 cm height onto the center of the glass plate. The plate should be spun in a horizontal plane, at a nearly constant number of revolutions per minute (rpm), until the solution dries. This experiment used a Hobby motor, capable of a maximum of 8300 rpm, which was operated at approximately 600 rpm with 0.3 A current.

Once dry the glass plate is removed from the spinner and submersed in distilled water. If the film does not cleanly float off the plate, a gentle nudge with a razor blade will free it. The thin film detectors thus produced will have an outside diameter of approximately 10 mm, can be lifted with tweezers, and secured to the scintillator rings with vacuum grease. These scintillators should be stored in a dust free environment. Experience has shown that scintillators produced by this technique survive long exposures to californium (several weeks at 1.5 inches from a  $0.75\ \mu\text{C}$  source) and continue to provide excellent resolution of the fission fragment spectrum.

## CHAPTER 4

### EXPERIMENTAL METHOD

As a result of this research, testing procedures and techniques have been developed that aid in insuring that accurate data collection is accomplished while making efficient use of the tester's time. The goal of this chapter is to outline the experimental methods used for data collection in order that others may duplicate this work. Before examining how data is collected let us first consider what data needs to be collected.

The primary purpose of this research remains the determination of the upset cross section versus LET curve which is essential to SEU studies. To better understand how, and most importantly why, the remaining experimental procedures are conducted one should first consider the sample SEU cross section curve presented in Figure 26.

### Sample SEU Cross Section

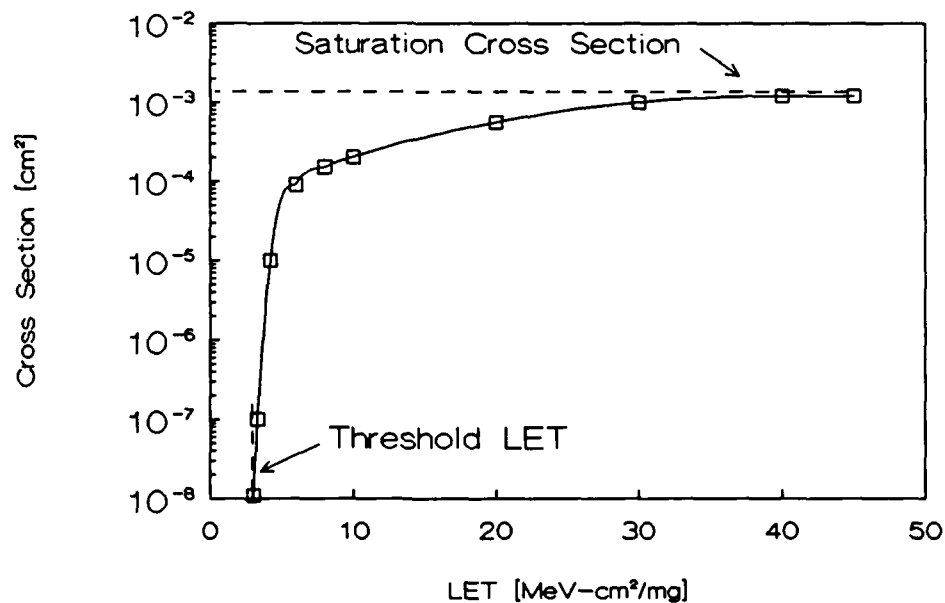


Figure 26. Sample SEU cross section curve.

The definition of the threshold LET varies with the experimentalist. JPL<sup>7</sup> defines it as that value of the LET where SEU first occur for fluences exceeding  $10^6$  ions/cm<sup>2</sup>. Others defines it as the LET value where the cross section is 10% of the saturation cross section.<sup>7</sup>

The following information is essential to the determination of this curve:

- 1) the thickness of the scintillators and absorbers
- 2) verification that the response of the scintillator is correlated with that of the SBD
- 3) the flux incident upon the DUT
- 4) the SEU error rate
- 5) the scintillator response for all fission fragments along with a means to identify those that caused errors
- 6) a method of data analysis to determine SEU cross sections
- 7) a means to determine fragment LET.

The manner in which these data are collected will be discussed in the appropriate sections throughout the rest of this chapter.

#### 4.1. Thickness Measurements

The thickness of the scintillators and attenuators is determined by measuring the energy loss of a collimated beam of the 6.119-MeV alpha particles emitted by the <sup>252</sup>Cf source used in our system. The following relationship applies:

$$\Delta E = \left[ \frac{dE}{dx} \right]_{avg} \Delta T$$

where:



$\Delta T$  is the scintillator thickness.

$\Delta E$  represents the energy loss as determined by the number of channels the alpha-particle peak shifts on the multi-channel analyzer when the alpha-particles impinge upon the surface barrier detector.

$\left(\frac{dE}{dx}\right)_{\text{avg}}$  = the average stopping power of the compound that constitutes the attenuator or scintillator as determined by Ziegler's method<sup>43</sup> as shown below :

$$\left(\frac{dE}{dx}\right)_{\text{avg}} = \sum (\text{relative abundance})(\text{stopping power})(\text{conversion to eV-cm}^2).$$

For our scintillator formulation the material density is  $1.032 \frac{\text{g}}{\text{cm}^3}$  and the hydrogen to carbon ratio is 1.104 hydrogen for each carbon<sup>44</sup>.

Thus,

$$\left(\frac{dE}{dx}\right)_{\text{avg}} = \left[ \left(\frac{1.104}{2.104}\right) \left(2.4 \frac{\text{MeV-cm}^2}{\text{mg}}\right) (1.674 \times 10^{-24} \frac{\text{g}}{\text{atom}}) + \left(\frac{1}{2.104}\right) \left(0.80 \frac{\text{MeV-cm}^2}{\text{mg}}\right) (19.95 \times 10^{-24} \frac{\text{g}}{\text{atom}}) \right]$$

$$\left(\frac{dE}{dx}\right)_{\text{avg}} = 9.69 \frac{\text{eV}}{10^{15} \frac{\text{atoms}}{\text{cm}^2}}$$

To convert back to units of  $\frac{\text{MeV}}{(\text{mg/cm}^2)}$  multiply the above by

$$\frac{0.6023 \times 10^{24} \frac{\text{atoms}}{\text{mole}}}{(\text{average atomic weight})}$$

$$\left(\frac{dE}{dx}\right)_{\text{avg}} = 9.69 \frac{\text{eV}}{10^{15} \frac{\text{atoms}}{\text{cm}^2}} \left[ \frac{0.6023 \times 10^{24} \frac{\text{atoms}}{\text{mole}}}{\left[ \left(\frac{1.104}{2.104}\right) \left(1 \frac{\text{g}}{\text{mole}}\right) + \left(\frac{1}{2.104}\right) \left(12 \frac{\text{g}}{\text{mole}}\right) \right]} \right]$$

$$\left(\frac{dE}{dx}\right)_{\text{avg}} = 0.937 \frac{\text{MeV-cm}^2}{\text{mg}}$$

Thickness measurements are most easily conducted by placing the scintillators, or attenuators, to be measured in the attenuator wheel. This test arrangement allows the testing of up to five items without having to open the chamber between the testing of

each item. Tests begin by allowing the unattenuated  $^{252}\text{Cf}$  alpha particles to bombard the SBD. This establishes the energy per MCA channel for the amplifier and conversion gain settings. It is best to have the gain adjusted so that the 6.119 MeV alpha peak will appear in a channel above 400 when 2048 channels are used on the MCA. Such an arrangement allows more precise measurement of the thickness of thinner scintillators. Each scintillator is tested, in turn, by rotating it into the alpha particle beam through the use of the manipulating rods that pass through the vacuum wall. Table 4 contains the results for the scintillators used to develop the SEU cross section versus LET curves that will be discussed in the results section.

Identification	Peak Channel ( $\alpha$ -particle)	Number of Channels Shifted	Thickness [ $\mu\text{g}/\text{cm}^2$ ]	Thickness [microns]
bare source	$471 \pm .5$	0	0	0
attenuator 2	$460 \pm .5$	$11 \pm .5$	$152.5 \pm 6.9$	$1.48 \pm 0.06$
8-11[4-75]	$458 \pm .5$	$13 \pm .5$	$180.2 \pm 6.9$	$1.74 \pm 0.06$
attenuator 3	$450 \pm .5$	$21 \pm .5$	$291.2 \pm 6.9$	$2.82 \pm 0.06$
7-14[2-100]	$431 \pm 1$	$40 \pm 1$	$554.6 \pm 13.9$	$5.37 \pm 0.13$
7-25[4-120]	$423 \pm 1$	$48 \pm 1$	$665 \pm 13.9$	$6.44 \pm 0.13$
attenuator 4	$402 \pm 1.5$	$69 \pm 1.5$	$956.7 \pm 20.8$	$9.27 \pm 0.20$

Table 4. The measured thickness of scintillators and attenuators.

A sample calculation is presented to show how the data in Table 4 were obtained for the 7-25[4-120] scintillator:

$$\Delta T = \frac{\Delta E}{\left[\frac{dE}{dx}\right]_{\text{avg}}} = \frac{\frac{6.119 \text{ MeV}}{471 \text{ channels}} \cdot 48 \text{ channels}}{0.937 \frac{\text{MeV-cm}^2}{\text{mg}}} = 665 \frac{\mu\text{g}}{\text{cm}^2} \quad \text{and} \quad \Delta T = \frac{665 \frac{\mu\text{g}}{\text{cm}^2}}{1.032 \frac{\text{g}}{\text{cm}^3}} = 6.44$$

microns.

Knowing the thickness of the scintillator and attenuators becomes an important factor in determining the LET delivered to the DUT by the different fission fragment groups. Additionally, by knowing the scintillator thickness one can calculate the kinetic energy of particles after their passage through the scintillator or attenuator and thus it is possible to calculate a range of penetration into the DUT for a particular fission fragment. These calculations will be discussed in greater detail later.

#### 4.2. Scintillator Versus SBD Calibration.

An essential requirement of this experiment is the determination of sufficient information about each fission fragment that transits the scintillator to allow the categorization of that particular fission fragment into a certain energy\mass\LET grouping. As discussed in the theory section, sufficient empirical and theoretical work exist to make such an undertaking plausible without a need to repeat the work of the pioneers in the TFD scintillator field.

However, the experience of scintillator manufacturing and testing during this research effort leads this author to conclude that a calibration of scintillator response versus that of a surface barrier detector should be performed after a new scintillator is made. The goal of such a calibration is to establish that, on a fragment-by-fragment basis, the scintillator and SBD responses correlate, i.e. that when the SBD detector detects a high- or low-energy particle the scintillator also detects an energy of the same

respective magnitude. Such a correlation is essential because, although the SBD response is accepted as a valid depiction of the  $^{252}\text{Cf}$  fission fragment spectrum, the actual SEU test arrangements preclude the concomitant bombardment of the SBD and the DUT. Thus, demonstrated proof that the scintillator response serves as a viable alternate representation of the  $^{252}\text{Cf}$  fission fragment spectrum is essential.

The SBD detector response to fission fragments from a  $^{252}\text{Cf}$  source is a widely recognized spectrum that typically appears in textbooks treating nuclear physics or nuclear instrumentation. In fact, recording the  $^{252}\text{Cf}$  fission fragment pulse-height spectrum serves as a standard test of heavy ion detector performance. Figure 27 shows the typical dual-humped  $^{252}\text{Cf}$  fission fragment pulse-height spectrum collected with a SBD during this research. The depicted spectrum is that of the unattenuated source.

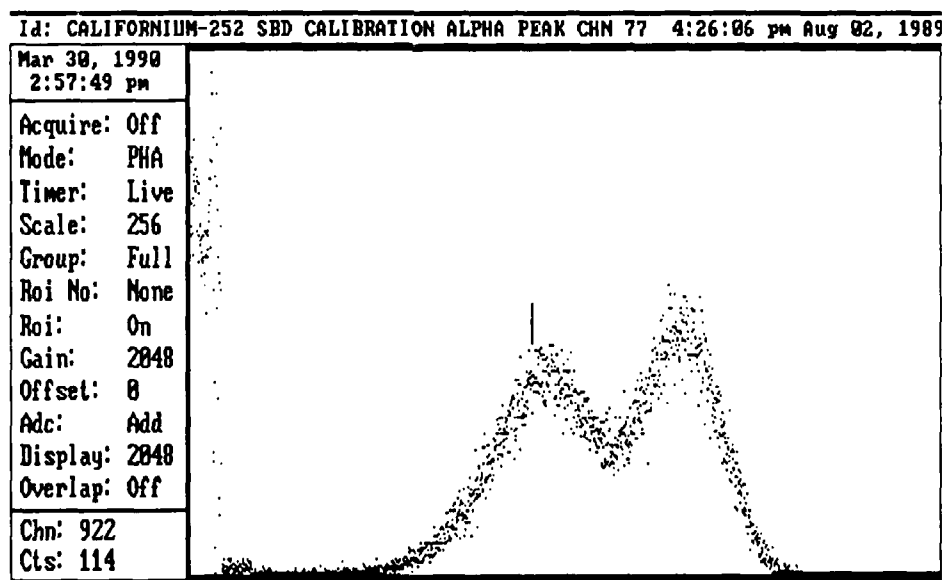


Figure 27. MCA pulse-height spectrum of unattenuated  $^{252}\text{Cf}$  fission fragments as detected by the SBD.

Figure 28 is a  $^{252}\text{Cf}$  fission fragment pulse-height spectrum detected by a TFD scintillator with a thickness of  $956\ \mu\text{g}/\text{cm}^2$ . Note that this spectrum also demonstrates a clear separation of the mass\energy groups as expected.

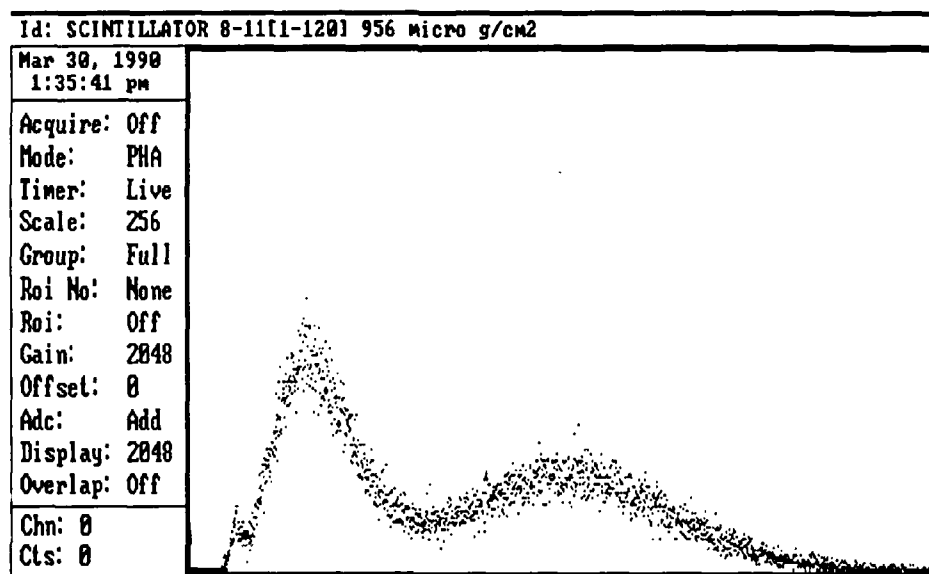


Figure 28. MCA pulse-height spectrum of  $^{252}\text{Cf}$  fission fragments as detected by a TFD scintillator of  $956\ \mu\text{g}/\text{cm}^2$  thickness.

Thus, separately, it is evident that this SEU test apparatus is capable of producing excellent representations of the  $^{252}\text{Cf}$  fission fragment spectrum for both the SBD and the scintillator detection schemes. Calibration of the scintillator response versus that of the SBD is accomplished by rotating the SBD into the fission fragment beam so that the fission fragments that transit the scintillator subsequently impinge upon the SBD. The pulse height responses from the nuclear instrumentation for group A and group B in Figure 25 are collected as data pairs and plotted as shown in Figure 29.

Note that the plot of the data pairs indicates that a fission fragment detected as a high-mass, low-energy fragment (low voltage) by the SBD is similarly categorized by the scintillator. Likewise, the correlation holds for low-mass, high-energy (high voltage) fragments. Additionally, an analysis of the frequency distribution of the scintillator pulse-height voltages yields the counts-per-channel distribution, shown as a dashed line in Figure 29, that shows that the dual-humped spectra that was expected, and observed, in Figures 27 and 28 exists in these data also. This correlation allows the SEU chamber to function and permits the tester to use the scintillator pulse-height information alone to characterize individual fission fragments.

### SBD vs. SCINTILLATOR CALIBRATION (SCINT 7-25[4-120] data taken 9-28-89)

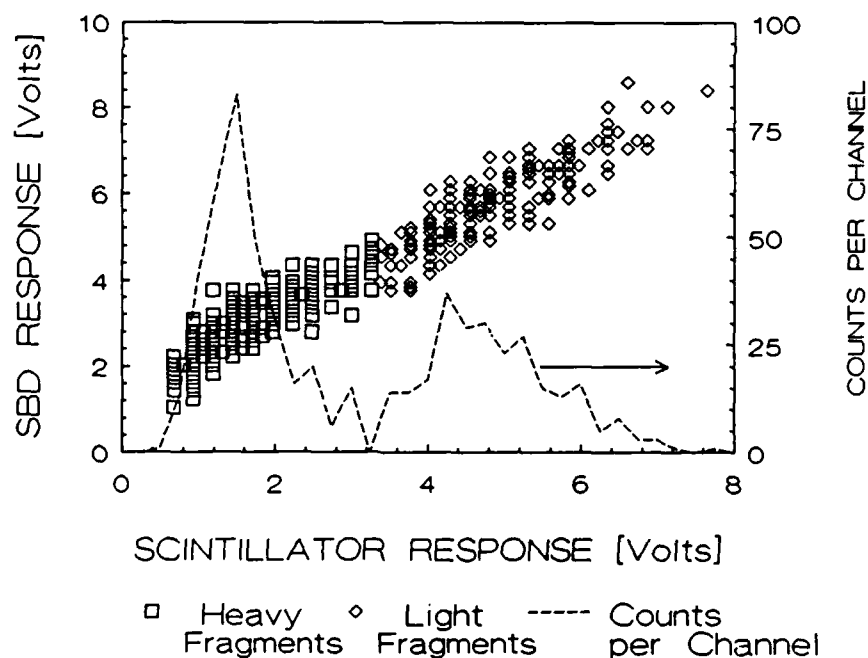


Figure 29. Calibration of a scintillator with the SBD.

### 4.3. The Overall SEU Cross Section

Each data point on an SEU cross section versus LET curve (Figure 26) is obtained by allowing a beam of particles to impinge upon a DUT and then determining the upset rate, the particle flux, and the LET (in the semiconductor material) of the bombarding particles. In accelerator testing the bombarding beam can be selected to provide a single elemental species of particles, at a specific LET, to establish one data point per beam type. Table 5 is an example of the typical beam parameters used in accelerator testing for SEU to allow sufficient variation of the LET to fully develop the cross section curve.

Ion	Energy [MeV]	LET (Si) [MeV-cm <sup>2</sup> /mg]
N	67	2.8
Ne	82	5.4
Ar	160	14
Kr	241	37
Kr	300	37

Table 5. Typical parameters for ions used in accelerator SEU testing.<sup>7</sup>

For this current research with <sup>252</sup>Cf, the SEU cross section curve is built by determining an overall upset cross section for each scintillator\attenuator combination transited by the beam, and developing separate upset cross sections for each energy\LET group that the fission fragment spectrum is divided into. For example, currently in our

testing scheme the fission fragment spectrum is divided into two energy groupings; the low-energy fission fragments and the high-energy fission fragments. Thus each overall SEU cross section can be divided into two distinct data points for the SEU cross section curve. A detailed discussion of this division is given in the section on the method of determining separate SEU cross sections.

The overall SEU cross section is defined as:

$$\sigma_{\text{overall}} = \text{overall SEU cross section} = \frac{\text{upset rate}}{\text{flux}}.$$

The upset rate is determined by merely dividing the total number of SEU errors recorded by the amount of time the test was conducted. The flux is measured by placing the SBD in the fission fragment beam and dividing the number of fission fragments per unit area by the exposure time. A collimated fission fragment beam of 0.3-cm diameter exists at the DUT location as a result of the chamber collimation system and thus an area of 0.283 cm<sup>2</sup> is used to calculate the number of fission fragments per unit area.

#### 4.4. Determining the Individual SEU Cross Sections

As discussed in the section on data collection and the microcomputer, the microcomputer collects data pairs that consist of:

- 1) the scintillation pulse-height voltage
- 2) whether or not an error occurred.

These data are collected throughout the testing of a particular DUT. Data analysis yields two distinct spectra, one of all fragment scintillation pulses and the other of those fragments that caused SEU. This ability to separate these spectra allows for the calculation of distinctly different upset cross sections for each mass (energy) group. Table 6 shows the results of the analysis of an experimental run that used scintillator



7-25[4-120] with attenuator 2 while testing the HM6516 2k x 8 SRAM. The voltage range of the scintillation response is divided into distribution bins of 0.5 volt increments. The recorded data are sorted and percentages for each voltage range calculated.

Scintillator Voltage Bin	Scintillation Frequency	% of All Scintillations	Error Frequency	% of All Errors
0.00	0	0	0	0
0.50	1	0.14	1	0.34
1.0	190	2.64	0	0
1.5	1680	23.3	16	5.48
2.0	1321	18.33	16	5.48
2.5	605	8.39	9	3.08
3.0	359	4.98	14	4.79
3.5	443	6.15	11	3.77
4.0	502	6.97	34	11.64
4.5	571	7.92	45	15.41
5.0	494	6.85	56	19.18
5.5	437	6.06	37	12.67
6.0	270	3.75	19	6.51
6.5	165	2.29	15	5.14
7.0	81	1.12	5	1.71
7.5	28	0.39	6	2.05
8.0	24	0.33	3	1.03
8.5	22	0.31	2	0.68
9.0	10	0.14	3	1.03
9.5	4	0.05	0	0
10	0	0	0	0

Table 6. Distribution and percentages for all scintillations and those that produce errors.

These percentages are then plotted versus the voltage range to establish the profile for all scintillations and a separate profile for those that caused errors. A plot of the data in Table 6 is shown in Figure 30 where the solid curve shows the pulse-height spectrum for scintillator pulses from all fission fragments, while the dashed curve is for fragments that produced upsets. The large second peak in the dashed curve indicates that the majority of SEU, for the scintillator\attenuator thickness in the example presented, was caused by the low-mass, higher-energy, fission fragments.

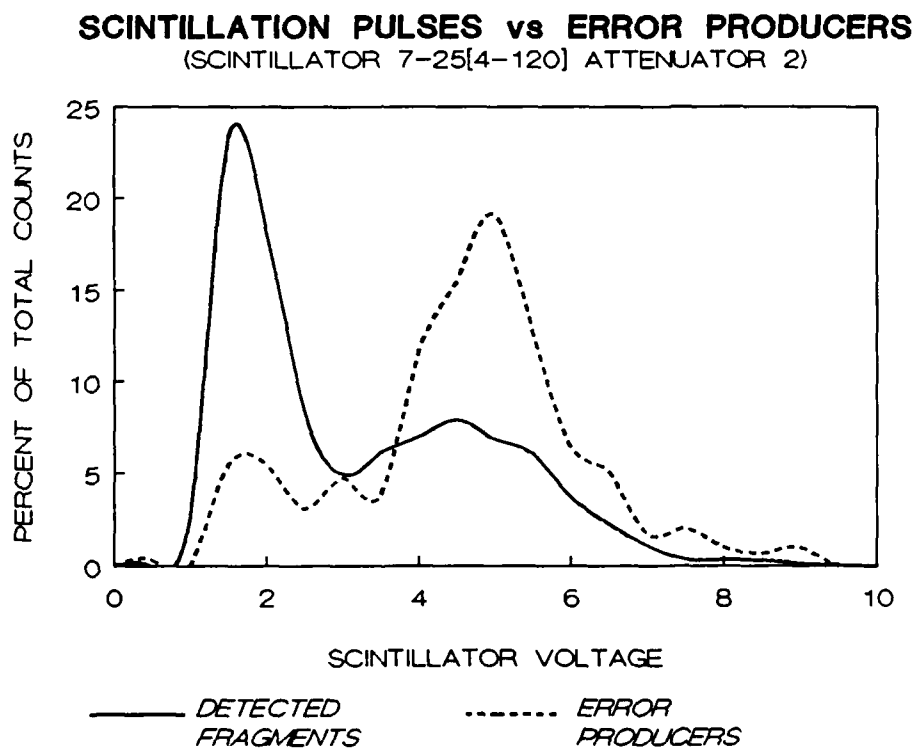


Figure 30. The distribution of all scintillations (solid line) and those that caused errors (dashed line) for a total attenuation of  $818 \mu\text{g}/\text{cm}^2$ .

In viewing the data in Table 6 and the graph in Figure 30 one quickly realizes that although this research effort only calculated upset cross sections for two energy

groups, it is possible to extend this technique to finer energy divisions for the californium spectrum.

For the heavy- and light-mass groups chosen for this research the following formulas show how the individual cross sections,  $\sigma_{\text{heavy}}$  and  $\sigma_{\text{light}}$ , are calculated:

$$\sigma_{\text{heavy}} = \frac{\sum \text{heavy error percentages}}{\sum \text{heavy scintillation percentages}} \sigma_{\text{overall}}$$

$$\sigma_{\text{light}} = \frac{\sum \text{light error percentages}}{\sum \text{light scintillation percentages}} \sigma_{\text{overall}}$$

For the example given in Table 6 and Figure 30 the overall cross section was  $7.30 \times 10^{-3} \text{ cm}^2$ . The scintillations and errors attributed to the heavy fission fragments went from 0 to 3 volts, resulting in 19.2% of the errors and 57.7% of all scintillations. Theoretically an unattenuated fission spectrum would yield an equal number of fission fragments in each energy group and the groups are easy to distinguish. The spectrum being analyzed has been attenuated by  $818 \mu\text{g}/\text{cm}^2$  of scintillation material, thus the energy spectrum has been compacted and shifted toward the lower energy region. This shifting combined with the need to choose an arbitrary dividing line between low-energy and high-energy regions accounts for the fact that 57.7% of this spectrum is considered low-energy. Throughout this experiment the arbitrary dividing line has been consistently chosen at the low point between the two peaks in the scintillation spectrum. For this particular case this results in:

$$\sigma_{\text{heavy}} = \frac{19.2}{57.7} (7.30 \times 10^{-3} \text{ cm}^2) = 2.42 \times 10^{-3} \text{ cm}^2$$

$$\sigma_{\text{light}} = \frac{80.8}{42.3} (7.30 \times 10^{-3} \text{ cm}^2) = 1.39 \times 10^{-2} \text{ cm}^2.$$

Thus two individual cross sections have been obtained. Plotting these points on the SEU cross section versus LET curve requires that the respective LET for each type of fragment be determined. The details of determining the fragment group LET are covered in the section on LET determination.

Figure 31 is a composite of scintillation spectrum distribution versus upset distribution for four different attenuations of the  $^{252}\text{Cf}$  spectrum. This plot illustrates the shifting of the error production to the light-mass high-energy group as the fragment energy attenuation increases. In each graph the solid line shows the distribution of scintillation pulse heights that correspond to the double humped  $^{252}\text{Cf}$  spectrum, and the dashed line shows the distribution of the fission fragments responsible for causing the SEU. Each graph's upper right hand corner shows the total thickness ( $\mu\text{g}/\text{cm}^2$ ) of scintillation and attenuation material that the fission fragments transited before impinging upon the DUT. As the  $^{252}\text{Cf}$  fragment energies decrease, the upset profile departs from following the  $^{252}\text{Cf}$  spectrum, as it does with the thinnest scintillator, to a profile that indicates that the bulk of the upsets are caused by the low-mass, higher-LET fragments.

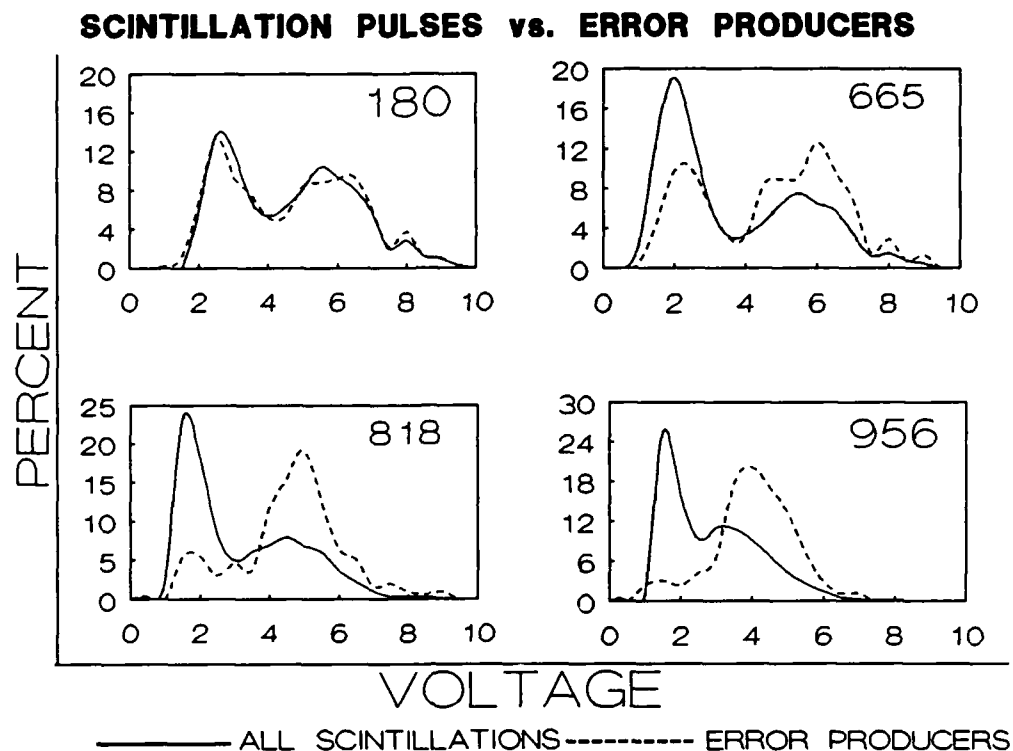


Figure 31. A composite of several data points that shows the effect of increased beam attenuation. The total thickness of the scintillator and attenuator material, in  $\mu\text{g}/\text{cm}^2$ , is displayed in the upper right hand corner of each plot.

#### 4.5. Method of Determining LET

The current analysis divides the detected fission spectrum into two energy groups; the heavy-mass, low-energy fission fragments and the light-mass, high-energy fission fragments. These groups can be represented by  $_{56}\text{Ba}$  and  $_{42}\text{Mo}$  respectively.  $_{56}\text{Ba}$ , with a mass of  $141.9 \pm 6.55$  AMU and an energy of  $79.4 \pm 8.23$  MeV, represents the mean value for the heavy fragments.  $_{42}\text{Mo}$ , with a mass of  $106 \pm 6.53$  AMU and an energy of  $103.7 \pm 5.48$  MeV, represents the mean value for the light fragments. These mean values and their associated standard deviations come from the work of Schmitt et

al.<sup>31</sup> Through the use of computer codes to transport these ions through the scintillator material, and into silicon, one can simulate our experimental process and determine: the ion energy upon departure from the scintillator, the kinetic energy upon entrance into the silicon, the  $dE/dx$  at the silicon surface, and the range the ion penetrates into the silicon.

The TRIM code provided by Ziegler<sup>43</sup> was used for these calculations. It is important to note that the TRIM code does not calculate LET. The TRIM code calculates the stopping power,  $dE/dx$ , of the ion in question at the surface of the material being bombarded. The linear energy transfer (LET) concept is a description of the rate of energy deposited into the absorber. As such it considers only the energy "locally imparted" to the absorber. It is different from stopping power in that LET refers to the average rate of energy deposited in a limited volume whereas stopping power refers to the average rate of energy lost by the bombarding particle no matter where in the absorber it is deposited. Incorrectly, this distinction is not systematically adhered to throughout the SEU radiation effects community. The accepted practice throughout the SEU radiation effects community is to analyze a device's hardness by examining the SEU cross section versus "LET" curve. To conform to convention, curves produced by this research will use the phrase "LET" in the title but the plotted values will be the total (electronic plus nuclear) stopping power,  $dE/dx$ , at the material surface. Table 7 compares the "LET" values used by various research groups. The columns labeled TRIM show the electronic and nuclear stopping powers obtained with the TRIM code by this research effort. Note that around a 10% difference can exist in the values used by different groups for the same ion.

ION	ENERGY [MeV]	LET JPL <sup>7</sup>	LET NASA <sup>45</sup>	LET Aerospace <sup>46</sup>	LET Browning <sup>54</sup>	TRIM $dE/dx_{elec}$	TRIM $dE/dx_{nuc}$
N	67	2.8	2.8	3.0	2.8	2.79	0.0017
Ne	82	5.45	5.81	6.0	5.78	5.72	0.0039
Ar	160	14	15.3	15.0	14.9	14.9	0.0123
Fe	100	28			28.2	29.6	0.0494
Kr	130	37	40.1		39.6	41.6	0.1030
Kr	300	37	38.8	40.7	38.6	40.3	0.0466

Table 7. A comparison of LET and  $dE/dx$  values used by various research groups.

Figure 32 depicts the results of using the TRIM code to determine the total  $dE/dx$  at the silicon surface after the passage of Mo or Ba through scintillators of different thickness. The error bars in Figures 32 and 33 represent the standard deviation in the LET and range obtained by transporting the mean fragment representing each energy group and its respective one-sigma mass and one-sigma energy variants through the total attenuation and combining the errors in quadrature. The one-sigma mass and one-sigma energy variants are from the work of Schmitt et al.<sup>31</sup>

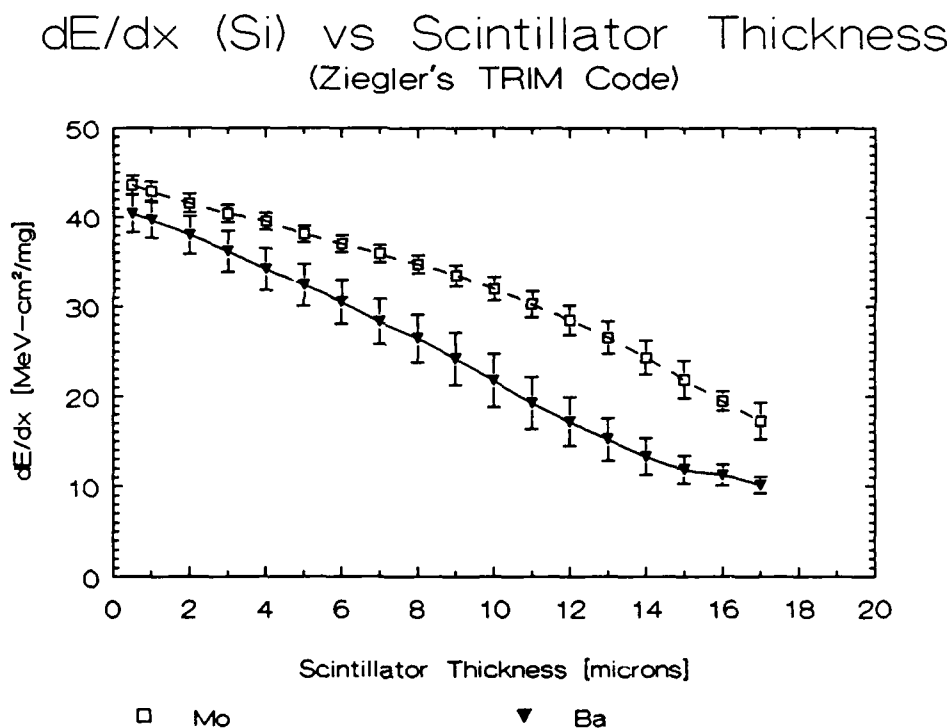


Figure 32.  $dE/dx$  at the surface of silicon as determined by the TRIM computer code. Mo and Ba were chosen to represent the light-mass and heavy-mass fission fragments group respectively, then transported through scintillators of varied thickness using initial energies and masses as discussed in the text.



Figure 33 shows the range of penetration into silicon after Mo or Ba has passed through scintillators of different thickness. The data used to plot Figures 32 and 33 provided the basis for determining the  $dE/dx$  values needed for the SEU cross section versus LET curve. The range of penetration was checked for the fission fragments to insure they penetrated to at least of depth of five microns. From the TRIM code it can be seen that scintillators up to 16 microns thick could be used and still have heavy fission fragments penetrate to about five microns. This would correspond to a surface  $dE/dx$  (Si) of around  $12 \text{ MeV-cm}^2/\text{mg}$ .

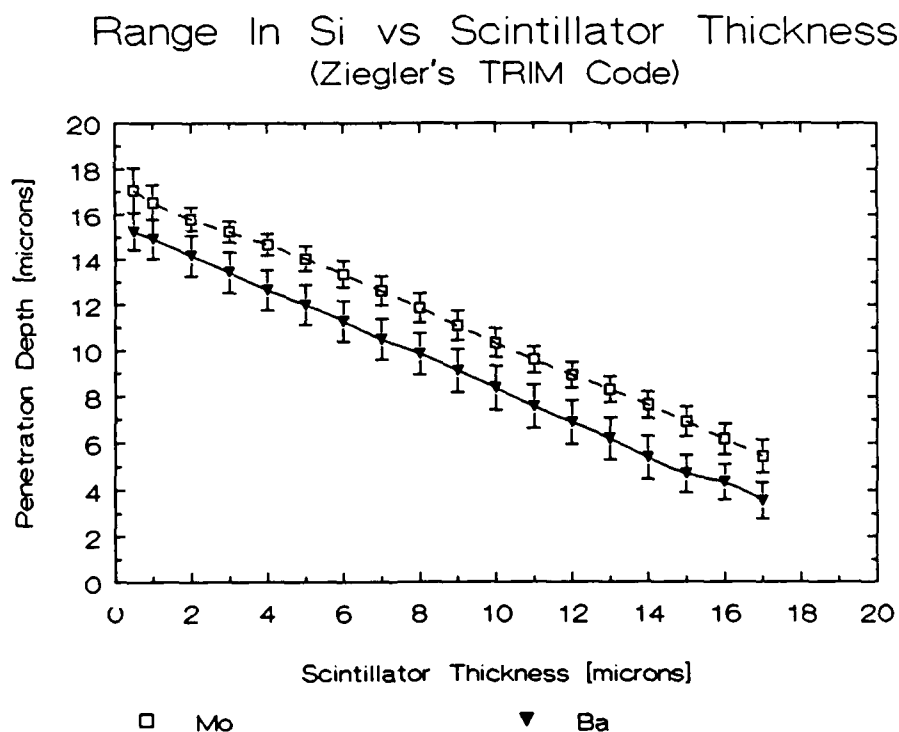


Figure 33. Range of penetration into silicon for Mo and Ba after transport through scintillators of different thickness.

As a final note it is essential to discuss the concept of effective LET. An effective LET is often used to relate the LET of different ion species and different angles of incidence to an equivalent LET for a heavy ion that penetrates the DUT at normal incidence. The accepted definition of effective LET is: the LET of a given ion divided by the cosine of the angle of penetration, with normal incidence being defined as zero degrees. This concept of effective LET will allow future designs of this SEU chamber to allow rotation of the DUT and allow exposures up to  $dE/dx$  (Si) of 70 MeV-cm<sup>2</sup>/mg. Thus, for devices which can be tested with ions with a vertical depth (i.e., depth below the surface of the chip) of 5 microns, <sup>252</sup>Cf can provide LET between 12 and 70 MeV-cm<sup>2</sup>/mg. This concludes the explanation of the experimental methods used in this research. The SEU cross section curves obtained during this investigation will be presented in the results section that follows.

## CHAPTER 5

### RESULTS

The testing involved in this research called for the development of the SEU cross section versus LET curve for several memory devices in order to demonstrate that this experimental system worked. The devices chosen for testing were the Harris Corporation HM6516, the Honeywell Corporation HC6116CHEC, and the Integrated Device Technology IDT6116. These devices are all 2kx8 SRAM, have been previously tested by the Jet Propulsion Laboratory, and are known to have relatively large upset cross sections. Since it is common for semiconductor manufacturers to improve their product line, while maintaining the same device nomenclature, we tested the same individual devices that the Jet Propulsion Laboratory had tested. Such an approach removed any uncertainty about a device's manufacturing pedigree while providing us devices with known saturation cross sections and threshold LET.

In the sections that follow the data collected for the different devices are presented. In each data set presented the total attenuation of the beam measurement contains the sum of the scintillator and attenuator thicknesses for each datum point. The standard deviations in the upset cross sections were obtained by treating the error process as a Poisson distribution. The standard deviation in the LET was obtained by transporting the mean fragment representing each energy group and its respective one-sigma mass and one-sigma energy variants through the total attenuation and combining the errors in quadrature as discussed in the experimental procedures chapter.

### 5.1. The Harris HM6516

As a result of JPL testing at the Berkeley cyclotron the HM6516 had a known saturation cross section of  $2.0 \times 10^{-2} \text{ cm}^2$  and a threshold LET of  $\leq 27 \text{ MeV-cm}^2/\text{mg}$ .<sup>47</sup>

Tables 8 and 9 contain the data obtained for the HM6516 during this research.

Total Beam Attenuation [ $\mu\text{g}/\text{cm}^2$ ]	Total Beam Attenuation [microns]	dE/dx Light Group [MeV-cm <sup>2</sup> /mg]	SEU Cross Section Light Group [cm <sup>2</sup> ]
$180 \pm 6.9$	$1.74 \pm 0.06$	$42 \pm 1.04$	$2.43 \times 10^{-2} \pm 6.67 \times 10^{-4}$
$332 \pm 9.7$	$3.22 \pm 0.08$	$40.2 \pm 0.98$	$2.28 \times 10^{-2} \pm 5.88 \times 10^{-4}$
$471 \pm 9.7$	$4.56 \pm 0.08$	$38.64 \pm 0.94$	$2.01 \times 10^{-2} \pm 6.94 \times 10^{-4}$
$554 \pm 13.9$	$5.37 \pm 0.13$	$37.7 \pm 0.91$	$1.73 \times 10^{-2} \pm 5.00 \times 10^{-4}$
$665 \pm 13.9$	$6.44 \pm 0.13$	$36.5 \pm 0.93$	$1.57 \times 10^{-2} \pm 4.25 \times 10^{-4}$
$707 \pm 15.5$	$6.85 \pm 0.15$	$35.9 \pm 0.97$	$1.36 \times 10^{-2} \pm 4.38 \times 10^{-4}$
$817 \pm 15.5$	$7.92 \pm 0.15$	$34.7 \pm 1.02$	$1.39 \times 10^{-2} \pm 3.80 \times 10^{-4}$
$956 \pm 20.8$	$9.26 \pm 0.20$	$33.1 \pm 1.17$	$3.81 \times 10^{-3} \pm 1.52 \times 10^{-4}$
$1053 \pm 21.9$	$10.2 \pm 0.24$	$31.6 \pm 1.35$	$2.32 \times 10^{-3} \pm 1.46 \times 10^{-4}$
$1208 \pm 21.9$	$11.7 \pm 0.24$	$29.0 \pm 1.57$	$1.63 \times 10^{-3} \pm 2.00 \times 10^{-4}$

Table 8. Essential data for the SEU cross section curve for the HM6516. These data are for the light-mass group.

Total Beam Attenuation [ $\mu\text{g}/\text{cm}^2$ ]	Total Beam Attenuation [microns]	$dE/dx$ Heavy Group [MeV-cm <sup>2</sup> /mg]	SEU Cross Section Heavy Group [cm <sup>2</sup> ]
$180 \pm 6.9$	$1.74 \pm 0.06$	$38.5 \pm 2.09$	$2.42 \times 10^{-2} \pm 5.93 \times 10^{-4}$
$332 \pm 9.7$	$3.22 \pm 0.08$	$35.7 \pm 2.30$	$2.04 \times 10^{-2} \pm 5.47 \times 10^{-4}$
$471 \pm 9.7$	$4.56 \pm 0.08$	$33.2 \pm 2.32$	$1.39 \times 10^{-2} \pm 4.15 \times 10^{-4}$
$554 \pm 13.9$	$5.37 \pm 0.13$	$31.7 \pm 2.31$	$1.18 \times 10^{-2} \pm 4.52 \times 10^{-4}$
$665 \pm 13.9$	$6.44 \pm 0.13$	$29.5 \pm 2.48$	$5.95 \times 10^{-3} \pm 3.06 \times 10^{-4}$
$707 \pm 15.5$	$6.85 \pm 0.15$	$28.6 \pm 2.50$	$7.33 \times 10^{-3} \pm 3.98 \times 10^{-4}$
$817 \pm 15.5$	$7.92 \pm 0.15$	$26.3 \pm 2.68$	$2.43 \times 10^{-3} \pm 1.87 \times 10^{-4}$
$956 \pm 20.8$	$9.26 \pm 0.20$	$23.6 \pm 2.97$	$4.89 \times 10^{-4} \pm 5.67 \times 10^{-5}$
$1053 \pm 21.9$	$10.2 \pm 0.24$	$21.3 \pm 2.92$	$5.51 \times 10^{-4} \pm 7.55 \times 10^{-5}$

Table 9. Essential data for the SEU cross section curve for the HM6516. These data are for the heavy-mass group.

Figures 34 and 35 show the SEU upset cross section versus LET curve plotted from these data. The curve fit is a third order polynomial. The saturation cross section obtained in this experiment is  $2.4 \times 10^{-2} \text{ cm}^2$  and the LET threshold is  $\leq 21 \text{ MeV-cm}^2/\text{mg}$ .

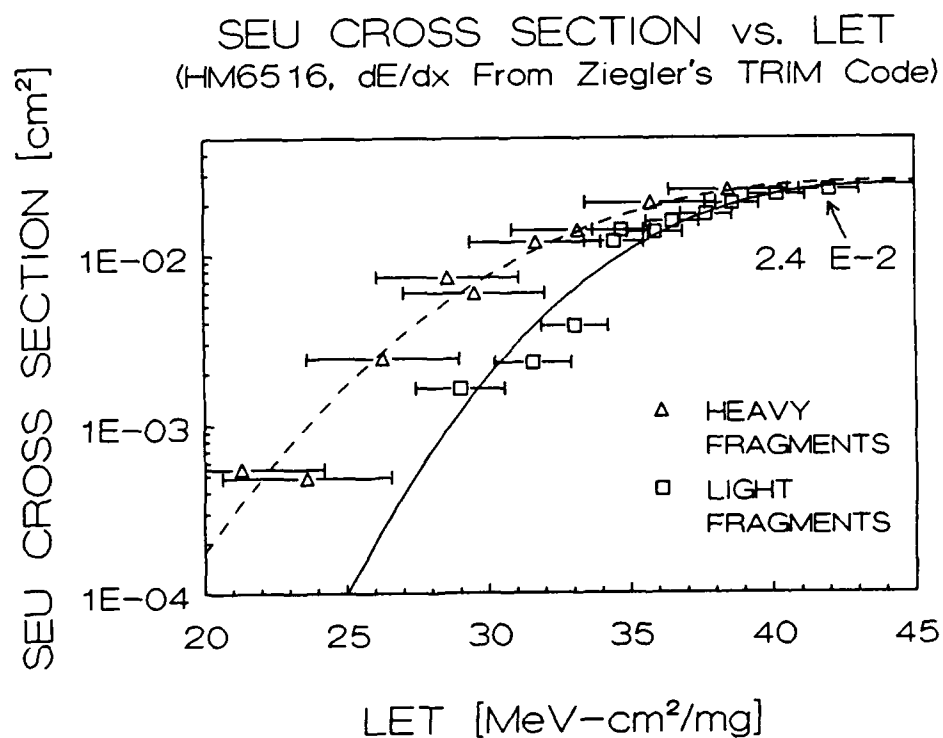


Figure 34. SEU cross section versus LET curve for the HM6516. The error bars show the dispersion in LET.

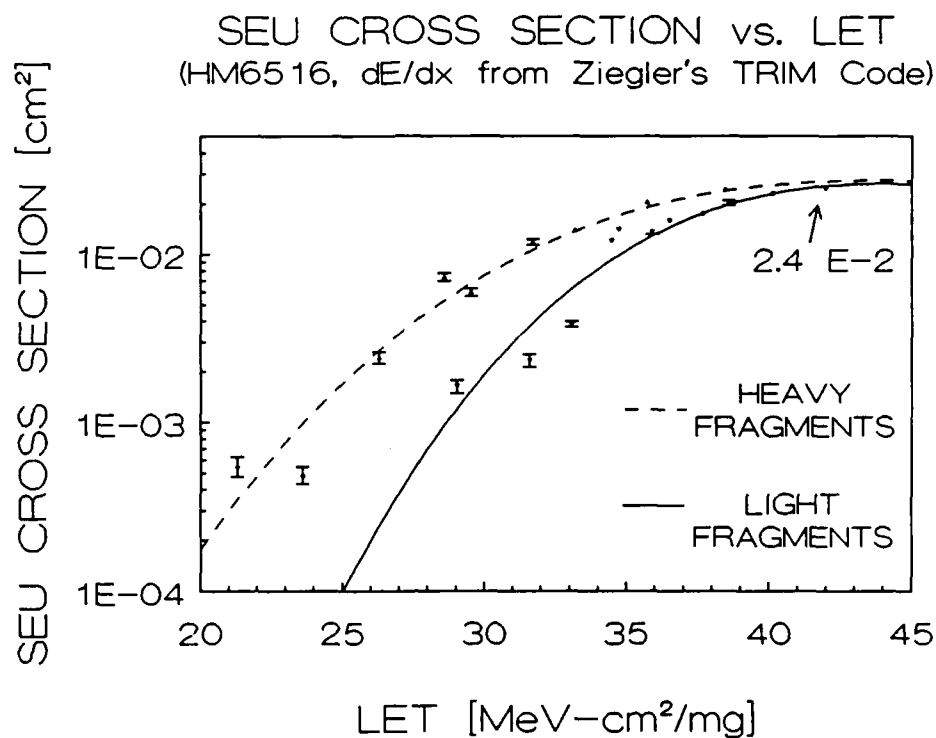


Figure 35. The SEU cross section versus LET for the HM6516. The error bars show the standard deviation in the cross section.

### 5.2. The Honeywell HC6116CHEC

The JPL tests on the HC6116CHEC showed it to have a SEU saturation cross section of  $6 \times 10^{-3} \text{ cm}^2$  and a LET threshold of  $27 \text{ MeV-cm}^2/\text{mg}$ .<sup>48</sup> Tests with our apparatus yielded a saturation cross section of  $7 \times 10^{-4} \text{ cm}^2$ . Extensive efforts were expended to verify proper alignment and operation of all equipment. Since all equipment appeared to work properly it was decided that the time required to develop a

cross section curve for this device was unreasonable with the current proof-of-principle equipment. Additionally, an examination of the raw data from the accelerator tests showed sufficient scatter in the data to include the possibility that the high upset cross section may have been an anomaly attributed to one part from one short duration exposure. To verify the our system's operational integrity a "softer" version of the 6116, the IDT 6116, was requested from JPL.

### 5.3. The IDT 6116

The JPL tests had revealed the IDT 6116 to have an SEU saturation cross section of  $1 \times 10^{-2} \text{ cm}^2$  and an LET threshold of  $3 \text{ MeV-cm}^2/\text{mg}$ .<sup>48</sup> Our test revealed a saturation cross section of  $1.4 \times 10^{-2} \text{ cm}^2$  and an LET threshold of  $\leq 17.2 \text{ MeV-cm}^2/\text{mg}$ . Tables 10 and 11 contain the data obtained for the IDT 6116 during this research.

Total Beam Attenuation [ $\mu\text{g}/\text{cm}^2$ ]	Total Beam Attenuation [microns]	dE\dx Light Group [ $\text{MeV-cm}^2/\text{mg}$ ]	SEU Cross Section Light Group [ $\text{cm}^2$ ]
$180 \pm 6.9$	$1.74 \pm 0.06$	$42 \pm 1.04$	$1.37 \times 10^{-2} \pm 7.38 \times 10^{-4}$
$554 \pm 13.9$	$5.37 \pm 0.13$	$37.7 \pm 0.91$	$8.57 \times 10^{-3} \pm 3.41 \times 10^{-4}$
$956 \pm 20.8$	$9.26 \pm 0.20$	$33.1 \pm 1.17$	$6.63 \times 10^{-3} \pm 1.68 \times 10^{-4}$
$1247 \pm 21.9$	$12.1 \pm 0.24$	$28.5 \pm 1.62$	$4.63 \times 10^{-3} \pm 1.72 \times 10^{-4}$
$1621 \pm 21.9$	$15.7 \pm 0.24$	$20.1 \pm 2.08$	$8.71 \times 10^{-4} \pm 7.18 \times 10^{-5}$

Table 10. Essential data for the SEU cross section curve for the IDT 6116. These data are for the light-mass group.



Total Beam Attenuation [ $\mu\text{g}/\text{cm}^2$ ]	Total Beam Attenuation [microns]	$dE/dx$ Heavy Group [MeV-cm <sup>2</sup> /mg]	SEU Cross Section Heavy Group [cm <sup>2</sup> ]
$180 \pm 6.9$	$1.74 \pm 0.06$	$38.5 \pm 2.10$	$9.17 \times 10^{-3} \pm 7.47 \times 10^{-4}$
$554 \pm 13.9$	$5.37 \pm 0.13$	$31.7 \pm 2.31$	$5.90 \times 10^{-3} \pm 3.17 \times 10^{-4}$
$956 \pm 20.8$	$9.26 \pm 0.20$	$23.6 \pm 2.97$	$7.24 \times 10^{-3} \pm 1.59 \times 10^{-4}$
$1247 \pm 21.9$	$12.1 \pm 0.24$	$17.2 \pm 2.72$	$3.03 \times 10^{-3} \pm 1.58 \times 10^{-4}$

Table 11. Essential data for the SEU cross section curve for the IDT6116. These data are for the heavy-mass group.

Figures 36 and 37 show plots of the SEU upset cross section versus LET data.

The lines in both graphs are spline fits to the data.

### SEU CROSS SECTION vs. LET (IDT 6116, $dE/dx$ from TRIM code)

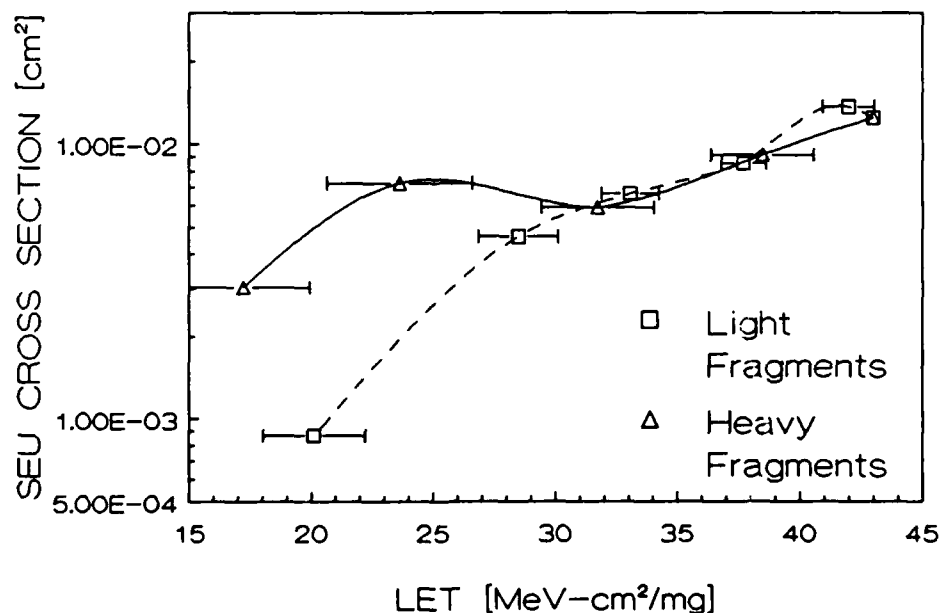


Figure 36. The SEU cross section versus LET for the IDT 6116. The error bars show the LET dispersion.

SEU CROSS SECTION vs. LET  
(IDT 6116, dE/dx from TRIM code)

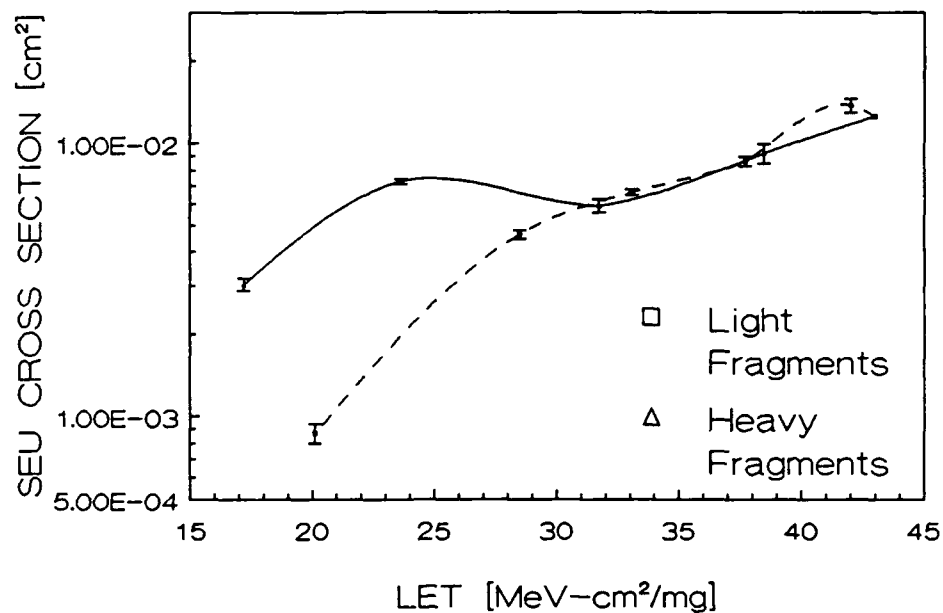


Figure 37. The SEU cross section versus LET for the IDT 6116. The error bars show the standard deviation in the cross section.

## CHAPTER 6

### DISCUSSIONS AND CONCLUSIONS

#### 6.1. Discussions

This research has resulted in a test apparatus that produces SEU upset cross section versus LET data that are in good agreement with the data obtained by JPL for the same devices during accelerator testing. The technique currently used allows the testing with LET from 17 to 43 MeV-cm<sup>2</sup>/mg. The key component of this system is the TFD scintillator system and it is noteworthy that scintillator response and durability have been excellent. Scintillator exposure has been as high as  $2.6 \times 10^6$  fission fragments per cm<sup>2</sup> without any detectable degradation in performance. The discussion that follows will highlight some key aspects of this research and propose suggestions for further research in the SEU arena.

In examining the SEU cross section curves presented in the previous chapter it is particularly interesting to note the structure that exists. For both the HM6516 and the IDT 6116 there appears a separation in the curves that indicates that for the same LET the heavy-mass fragments are causing more upsets than the light-mass fragments. Concern that this was an anomaly of our cross section separation technique abated when evidence was found that such experimental observations of the separation of SEU cross section versus LET curves by ion species have been reported by others.<sup>49,50,51,52,53</sup> The work of Sexton et al.<sup>49</sup> is shown in figure Figure 38. Sexton et al. explain the leftward shift of the cross section curves for increasing ion mass by stating that more charge is collected from a strike by a heavier ion. Stapor et al.<sup>52</sup> proposed that a suggested mechanism for such a phenomenon is that as the ion mass increases so also increases the cross sectional area of the plasma track. Such an increase in plasma track cross sectional area results in an effective lowering of plasma density and decreased recombination.

This would essentially raise the amount of charge collected along the ion track. Sexton et al.<sup>49</sup> proposed a more intuitively appealing explanation that relied on increasing plasma density with increasing ion mass. They proposed that an increase in plasma density would extend the effective funnel length thus resulting in an increase in drift current collected. If the latter model is valid than such curve separations should not be evident in the testing of SOI technologies.

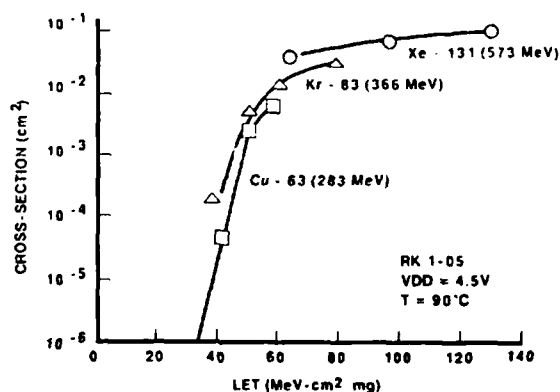


Figure 38. Dependence of measured cross section on ion species during exposure.<sup>49</sup>

At this juncture it necessary to state that both of the above explanations support the concept of increased error rate for increased ion mass and that further work to produce a detailed physics based model is warranted. Current accelerator SEU testing techniques rely on the ability to achieve LET equivalence among ion species by varying ion energy and the angle of incidence. If the current concept of LET equivalence is in error, than our accepted testing techniques do not properly estimate the error rates that can be expected in the actual cosmic environment. Further investigations into this matter should involve computer simulations to determine if an improved model of

effective LET can be determined by considering effective LET as a function of incident angle, ion species mass, effective charge, range of penetration, track radial extent, and plasma density and conductivity.

In viewing the SEU cross section plots from this research, one should also note that the structure in the IDT 6116 curve could indicate that p-channel and n-channel devices in that SRAM have different upset cross sections. To further investigate this phenomenon device layout information must be obtained from the manufacturer and a simulation code capable of three-dimensional simulation of ion interactions with semiconductor materials will be needed.

To improve the capabilities of the  $^{252}\text{Cf}$  based system that resulted from this research the following should be considered:

- 1) procurement or construction of faster data acquisition equipment
- 2) test the use of attenuators after the scintillator thus allowing a single scintillator to remain in the center of the light pipes and eliminating the frequent movement of light pipes to emplace new scintillators
- 3) use of a memory tester that can also provide information on the address and physical location of errors
- 4) the DUT card section of the chamber should be redesigned to allow the DUT to rotate so that fission fragments can strike the DUT at other than normal incidence. Such a modification would allow the system to reach effective LET values up to  $70 \text{ MeV-cm}^2/\text{mg}$ .

## 6.2. Conclusions

The result of this research is that a test device for microelectronics has been developed to measure single event upset cross section versus linear energy transfer by using  $^{252}\text{Cf}$  fission fragments in conjunction with thin-film scintillators. Traditionally

the testing of microelectronics for single event sensitivity involved actual exposure to the cosmic ray environment by high altitude flight programs or the simulation of the cosmic ray environment through the use of heavy ion beams produced by accelerators. These simulations are expensive and of limited access, thus alternatives have been sought.

The first efforts to use  $^{252}\text{Cf}$  for SEU testing involved placing a  $^{252}\text{Cf}$  source in an evacuated chamber, bombarding the device under test, and calculating a single upset cross section that is presumably was the saturation cross section. Such tests do not adequately address the uncertainties associated with the LET dispersion, and fail to usefully characterize the SEU threshold and saturation cross section of a device because there is no means to provide the SEU cross section versus LET curve. This system developed in this research effort addresses these shortcomings.

The key operational concept of this system is the ability to measure the energy of each heavy ion as it passes through a thin organic scintillator on the way to the device under test (DUT), and tag DUT upsets with the responsible fission fragment.

Data analysis yields two distinct spectra, one of all fragment scintillation pulses and the other of those fragments that caused SEU. This ability to separate these spectra allows for the calculation of distinctly different upset cross sections for each energy group. Although this work determined upset cross sections for two fragment energy groups, this technique can be readily extended to finer energy group divisions for the californium spectrum.

The SEU cross section for several 2kx8 SRAM have been measured with this test device over the LET range from 17-43 MeV-cm<sup>2</sup>/mg. The saturation cross sections and threshold LET values are in good agreement with the results from accelerator measurements. This californium-based device is quite small and fits onto a bench top.

It provides a convenient and inexpensive supplement, or alternative, to accelerator and high-altitude SEU testing.

## REFERENCES

1. D. Binder, E. C. Smith, and A. B. Holman, "Satellite Anomalies From Galactic Cosmic Rays," IEEE Trans. Nucl. Sci., Vol. NS-22, No. 7, 2675 (1975).
2. A. L. Ward, "Avalanching In Single-Event-Upset Charge Collection in Semiconductor Diodes," IEEE Trans. Nucl. Sci., Vol. NS-33, No.6, 1552 (1986).
3. E. R. Berger, M. House, G. Manzo and A. H. Taber, "Single Event Upsets in Microelectronics: Third Cosmic Ray Upset Experiment," IBM Technical Directions, Vol. 11, No. 1, 33 (1985).
4. James E. Gover and John S. Browning, "Radiation-Hardening Systems Considerations: Electrical Systems and Radiation Environments," Sandia National Laboratories, SAND86-1737, 38 (1987).
5. G. C. Messenger and M. S. Ash, The Effects Of Radiation On Electronic Systems, Van Nostrand Reinhold Co, p. 296-314, 1986.
6. T. P. Ma and Paul V. Dressendorfer, "Ionizing Radiation Effects In MOS Devices And Circuits," John Wiley & Sons, New York, p. 489, 1989.
7. D. Nichols, M. Huebner, W. Price, L. S. Smith, and James R. Cross, "Heavy Ion Induced Single Event Phenomena (SEP) Data for Semiconductor Devices from Engineering Testing," JPL Publ. 88-17 (1988).
8. W. A. Kolasinski, J. B. Blake, J. K. Anthony, W. E. Price, E. C. Smith, "Simulation of Cosmic-Ray-Induced Soft Errors and Latchup in Integrated-Circuit Computer Memories," IEEE Trans. Nucl. Sci., Vol. NS-26, 5087 (1979).
9. J. S. Browning, "Single-Event Correlation Between Heavy Ions And Cf-252 Fission Fragments," Nucl. Instr. and Meth., B45, 714 (1990).



10. J. H. Stephen, T. K. Sanderson, D. Mapper and J. Farren, "A Comparison Of Heavy Ion Sources Used In Cosmic Ray Simulation Studies Of VSLI Circuits," IEEE Trans. Nucl. Sci., Vol. NS-31, No. 6, 1069 (1984).
11. J. T. Blandford and J. C. Pickel, "Use Of Cf-252 To Determine Parameters For SEU Rate Calculation," IEEE Trans. Nucl. Sci., Vol. NS-32, No. 6, 4282 (1985).
12. T. K. Sanderson, D. Mapper, J. H. Stephen, and J. Farren, "SEU Measurements Using Cf-252 Fission Particles, On CMOS Static RAMs, Subjected To A Continuous Period Of Low Dose Rate Co-60 Irradiation," IEEE Trans. Nucl. Sci., Vol. NS-34, No. 6, 1287 (1987).
13. R. Velazco, A. Provost-Grellier, T. Chapuis, M. Labrunee, D. Falguere, R. Koga, "Comparison Between Californium and Cyclotron S.E.U. Tests," IEEE Trans. Nucl. Sci., Vol. NS-36, No. 6, 2388 (1989).
14. R. C. Block and M. C. Becker, "An Improved 252Cf Single-Event-Upset Simulation Technique for Testing Microelectronics," Trans. Am. Nucl. Soc., 54, 18 (1987).
15. T. V. Rajeevakumar, Nicky C. Lu, W. H. Henkels, W. Hwang, R. Franch, "A New Failure Mode of Radiation-Induced Soft Errors in Dynamic Memories", IEEE Electron Device Letters, Vol. 9, No. 12, 644-646 (1988).
16. R. Koga and W. A. Kolasinski, "Effects of Heavy Ions on Microcircuits In Space: Recently Investigated Upset Mechanisms", IEEE Trans. Nucl. Sci., Vol. NS-34, No. 1, 46 (1987).
17. T. F. Wrobel, "On Heavy Ion Induce Hard-Errors In Dielectric Materials", IEEE Trans. Nucl. Sci., Vol. NS-34, No.6, 1262-1268 (1987).

18. F. B. McLean and T. R. Oldham, "Basic Mechanisms of Radiation Effects in Electronic Materials and Devices." U.S. Army Laboratory Command, Harry Diamond Laboratories, p. 52, 1987.
19. Z. Shanfield, M. M. Moriwaki, W. M. Digby, and J. R. Srou, "Characteristics Of SEU Current Transients And Collected Charge In GaAs And Si Devices", IEEE Trans. Nucl. Sci., Vol. NS-32, No. 6, 4104-4109 (1985).
20. T. R. Oldham, F. B. McLean, and J. M. Hartman "Revised Funnel Calculations for Heavy Particles With High  $dE/dx$ ", IEEE Trans. Nucl. Sci., Vol. NS-33, No. 6, 1646-1650 (1986).
21. F. B. McLean, "Interactions Of Hazardous Environments With Electronic Devices", 1987 IEEE NSRE Short Course, p. 54-55, 1987.
22. J. P. Kreskovsky and H. L. Grubin, "Simulation Of Single Radiation Particle Tracks In Silicon And Gallium Arsenide Semiconductor Devices," DNA-TR-86-295, p. 1-9, 1986.
23. H. L. Grubin, J. P. Kreskovsky, and B. C. Weinberg, "Numerical Studies Of Charge Collection And Funneling In Silicon Devices," IEEE Trans. Nucl. Sci., Vol. NS-31, No. 6, 1161 (1984)
24. J. S. Fu, R. Koga, W. A. Kolasinski, "Processing Enhanced SEU Tolerance In High Density SRAMS", IEEE Trans. Nucl. Sci., Vol. NS-34, No. 6, 1322-1325 (1987).
25. W. R. Dawes, Jr., "Radiation Effects Hardening Techniques", Sandia National Laboratory, Tutorial Short Course IEEE 1985 Nuclear and Space Radiation Effects Conference, 40-45 (1985).

26. H. T. Weaver, "An SEU Tolerant Memory Cell Derived From Fundamental Studies Of SEU Mechanisms In SRAM", IEEE Trans. Nucl. Sci., Vol. NS-34, No.6, 1281 (1987).
27. G. F. Knoll, "Radiation Detection And Measurement," John Wiley And Sons, New York, p.13-14, 1979.
28. M. A. Preston and R. K. Bhaduri, "Structure Of The Nucleus," Addison-Wesley Publishing Co., Massachusetts, p. 555, 1982.
29. E. Segre, "Nuclei And Particles," The Benjamin/Cummings Publishing Co., Massachusetts, p.572-584, 1977.
30. R. Eisberg and R. Resnick, "Quantum Physics Of Atoms, Molecules, Solids, Nuclei, And Particles," John Wiley & Sons, New York, p. 602-207, 1985.
31. H. W. Schmitt, W. E. Kiker, and C. W. Williams, Precision Measurements Of Correlated Energies and Velocities Of  $^{252}\text{Cf}$  Fission Fragments, Phys. Rev., 137, B837 (1965).
32. M. L. Muga, "A Versatile dE/dx Detector For Heavy Mass Nuclear Particles," Nucl. Instr. and Meth. 95, 349 (1971).
33. M. L. Muga and G. Griffith, "Response Of Thin Film Scintillator Detector To Light And Heavy Ions," Nucl. Instr. and Meth., 109, 289 (1973).
34. W. J. McDonald, A. I. Kilvington, C. J. Batty and J. L. Weil, "Identification Of Fission Activity Using Thin-Film Detectors," Nucl. Instr. and Meth., 115,185 (1974).
35. N. N. Ajitanand and K. N. Iyengar "On The Technique Of High Quality Thin Film Scintillators," Nucl. Instr. and Meth., 133,71 (1976).

36. I. Kanno and Y. Nakagome, "A New Model Of Luminescence Production In A Very Thin Plastic Scintillator Film," Nucl. Instr. and Meth., A244, 551 (1986).
37. Kanno and Y. Nakagome, "Response Characteristics Of Thin Film Detectors To Fission Fragments," Nucl. Instr. and Meth., A251, 108 (1986)
38. J. F. Ziegler, J. P. Biersack, U. Littmark, "The Stopping And Range Of Ions In Solids, Pergamon Press," New York, 1985.
39. R. D. Evans, "The Atomic Nucleus," McGraw-Hill Book Company, New York, p. 670, 1955.
40. J. Lindhard, M. Scharff, and H. E. Schiott, "Range Concepts And Heavy Ion Ranges," Mat. Fys. Medd. Dan. Vid. Selsk. 33, 14 (1963).
41. G. Forcinal, P. Siffert, and A. Coche, "Pulse-Height Defects Due To Nuclear Collisions, Measured With A Thin-Window Silicon Surface Barrier Detector," "Semiconductor Nuclear-Particle Detector and Circuits," National Academy Of Sciences, Washington, D.C., p. 37, 1969.
42. Isotope Products Laboratories, 1800 N. Keystone Street, Burbank, CA 91504
43. J. F. Ziegler, "Handbook of Stopping Cross-Sections For Energetic Ions In All Elements," Pergamon Press, New York, p. 40, 1980.
44. B. Wilson, Nuclear Enterprises, (Private Communications).
45. E. G. Stassinopoulos, J. M. Barth, and T. M. Jordan, "Cosmic Ray Heavy Ion LET Mapping For Aluminum, Silicon, and Tissue Targets," NASA Reference Pub. 1180 (1987).
46. R. Koga, W. A. Kolasinski, M. T. Mara, and W. A. Hanna, "Techniques Of Microprocessor Testing And SEU-Rate Prediction," IEEE Trans. Nucl. Sci., Vol. NS-32, No. 6, 4219 (1985).

47. D. Nichols, JPL, (Private Communication).
48. D. K. Nichols, L. S. Smith, G. A. Soli, R. Koga, W. A. Kolasinski, " Latest Trends In Parts SEP Susceptibility From Heavy Ions," Trans. Nucl. Sci., Vol. NS-36, 2388 (1989).
49. F. W. Sexton, J. S. Fu, R. A. Kohler, and R. Koga, "Characterization Of A Hardened CMOS 64k and 256k SRAM," IEEE Trans. Nucl. Sci., Vol 36, No. 6, 2311 (1989).
50. E. G. Stassinopoulos, G. J. Brucker, O. Van Gunten, H. S. Kim, "Variation In SEU Sensitivity Of Dose-Imprinted CMOS SRAMS," IEEE Trans. Nucl. Sci., Vol 36, No. 6, 2330 (1989).
51. T. L. Criswell, D. L. Oberg, J. L. Wert, P. R. Measel, and W. E. Wilson, "Measurements Of SEU Thresholds And Cross Sections At Fixed Angles," IEEE Trans. Nucl. Sci., Vol 34, No. 6, 1316 (1987).
52. W. J. Stapor, P. T. McDonald, A. B. Campbell, A. R. Knudson, and B. G. Glagola, "Charge Collection In Silicon For Ions Of Different Energy But Same Linear Energy Transfer (LET)," IEEE Trans. Nucl. Sci., Vol 35, No. 6, 1585 (1988).
53. R. C. Martin, N. M. Ghoniem, Y. Song, and J. S. Cable, "The Size Effect Of Ion Charge Tracks On Single Event Multiple Bit Upset," IEEE Trans. Nucl. Sci., Vol 34, No. 6, 1305 (1987).
54. J. S. Browning, "Technical Perceptions," TePe Enterprises, Albuquerque, New Mexico (1986).
55. C. M. Hsieh, P. C. Murley, and R. R. O'Brien, "A Field-funnelling Effect on the Collection of Alpha-Particle-Generated Carriers in Silicon Devices," IEEE Trans. Elec. Dev., Vol. EDL-2, No.4, 103 (1981).

56. C. Hu, "Alpha-Particle-Induced Field and Enhanced Collection of Carriers," IEEE Elect. Dev. Lett., EDL-3, No.2, 31 (1982).

## Appendix

This is the computer program that controls data collection and storage.

```
1  PRINTER IS CRT
! the scope is defined as the location for information printout during the experimental
run
10  ASSIGN @Scope TO 708
!the digital oscscope will be addressed as number 708
20  OPTION BASE 1
30  ALLOCATE REAL Pulse(16000,2)
! this sets up the memory storage matrix for scintillation and error information
40  OUTPUT @Scope;"rqs 1040 HEADER OFF"
50  ON INTR 7 GOTO Getmax
! the computer has told the scope to go to subroutine "Getmax" when intr 7(trigger) is
received
60  ENABLE INTR 7;2
70  DISABLE INTR 7
! steps 40 through 70 explain to the scope how and when to respond to the computer
80  FOR I=1 TO SIZE(Pulse,1)
90  ENABLE INTR 7
95  OUTPUT @Scope;"DIG 1,2"
! the scope has been told to digitize the information on channel 1 and channel 2 when it
is triggered.
110 Loc1: GOTO Loc1
130 Back: PRINT I,Pulse(I,1),Pulse(I,2)
140  NEXT I
! this tells the scope to print the information to the screen and wait for the next
triggering event
150  ! done put scope in run
160  OUTPUT @Scope;"run"
161  LOCAL @Scope
163  MASS STORAGE IS "\blp:DOS,C"
! the computer is setting up to store the data on the hard disk and will ask the operator
for a file name
164  File$=""
165  INPUT "ENTER NAME OF OUTPUT FILE: ",File$
166  CREATE File$,1
167  ASSIGN @Path TO File$;FORMAT ON
168  FOR Row=BASE(Pulse,1) TO SIZE(Pulse,1)+BASE(Pulse,1)-1
170  OUTPUT @Path USING "MDD.DD,1X,MDD.DD";Pulse(Row,1),Pulse(Row,2)
172  NEXT Row
175  PRINT "YOUR DATA OUTPUT FILE HAS BEEN SAVED "
176  STOP
! below is the subroutine that sends the pulse height maximum information to the
computer
180 Getmax: DISABLE INTR 7
```

```
200     OUTPUT @Scope;"MEAS;VMAX 1 ?"  
210     ENTER @Scope USING "K";Pulse(I,1)  
220     OUTPUT @Scope;"MEAS;VMAX 2 ?"  
230     ENTER @Scope USING "K";Pulse(I,2)  
241     Stat=SPOLL(@Scope)  
251     GOTO Back  
270 END
```